Constraints on dark matter models using a fast simulation of the ATLAS detector

by

Samantha H. Taylor
B.Sc., University of Winnipeg, 2018

A Thesis Submitted in Partial Fulfillment of the
Requirements for the Degree of

MASTER OF SCIENCE

in the Department of Physics and Astronomy

Constraints on dark matter models using a fast simulation of the ATLAS detector

by

Samantha H. Taylor
B.Sc., University of Winnipeg, 2018

Supervisory Committee

Dr. M. Lefebvre, Supervisor
(University of Victoria Department of Physics and Astronomy)

Dr. R. Sobie, Departmental Member
(University of Victoria Department of Physics and Astronomy)

Supervisory Committee

Dr. M. Lefebvre, Supervisor
(University of Victoria Department of Physics and Astronomy)

Dr. R. Sobie, Departmental Member
(University of Victoria Department of Physics and Astronomy)

ABSTRACT

Data collected at the LHC are analyzed by the ATLAS collaboration for evidence of dark matter. In this thesis, a fast simulation of the ATLAS detector response using the DELPHES software is assessed for dark matter models with a leptonically decaying Z boson and a pair of dark matter particles in the final state. Limits for the Two Higgs Doublet plus pseudoscalar dark matter model are obtained using simplified systematics, and found to be nearly indistinguishable to limits obtained using the more complex standard ATLAS analysis.

Contents

List of Tables

List of Figures

Acknowledgements

I would like to thank:

My parents, I don't know where I would be without you. You are the reason I am who I am today. Thank you for everything.

Derrick, for your unwavering love and support. You believed in me when I didn't believe in myself.

Rafi, Kasey and John, thank you for all of the study sessions, DnD nights, coffee dates, and countless laughs.

Michel, for your neverending patience and guidance. I couldn't have done this without your counsel.

Dr. Andrew Frey, for your guidance throughout my undergraduate studies. I wouldn't be here today without your encouragement.

Dr. Randall Sobie, for being on my supervisory committee.

Dedication

To Mom and Dad.

Declaration

The Mono-Z dark matter search is part of the larger ATLAS Higgs working group and shares the same final state as the invisible Higgs search. As such, the background estimates and analysis techniques used are shared between groups. Thus, the background estimates used are provided by other analysts. The main analyst for the Mono-Z search is Kayla McLean, who provided the main results using the full ATLAS simulation. The following describes the author's contributions to the analysis.

Analysis contributions

- Signal event generation using DELPHES fast simulation of the ATLAS detector response.
- Optimization of the DELPHES parameter card to closely reproduce ATLAS results.
- Implementing a substitute kinematic cut for the missing transverse momentum significance, which is not defined within DELPHES.
- Normalization and comparison of kinematic distributions to those obtained from the full analysis.
- Limit setting for the dark matter models of interest and comparison to those obtained from the full analysis.
- Using HISTFITTER to perform a frequentist profile likelihood test and obtain expected and experimental limits.

Glossary

$\vec{\not{E}}_T$ Missing transvese momentum.

H_T Sum of scalar transverse momenta.

$\mu_{\mathbf{up}}$ Upper limit on the signal strength μ.

ΔR Angular separation between two particles.

η Pseudorapidity, defined as $\eta = -\ln\big(\tan\left(\frac{\theta}{2}\right)\big)$.

m_{TZZ} ZZ transverse mass. The discriminant variable of this analysis.

fb Femtobarn. A unit of area equal to 10^{-43} m^2.

2HDMa Two Higgs doublet dark matter model with a pseudoscalar mediator a.

ATLAS A Toroidal LHC ApparatuS. A multipurpose detector at the LHC.

CERN The European Organization for Nuclear Research.

Delphes A fast simulation software to emulate cylindrical detectors.

ECAL Electromagnetic calorimeter.

Hadronization The process of gluons and quarks combining to create hadrons.

HCAL Hadronic calorimeter.

HepMC Monte Carlo event record file.

HistFitter A software package used for the statistical treatment of the data.

ID Inner detector. A high-sensitivity detector located in the innermost part of the ATLAS detector.

Jet A stream of particles formed by the hadronization of gluons and/or quarks.

LHC The Large Hadron Collider.

MadGraph A Monte Carlo generator for hard scattering processes.

MS Muon spectrometer. Detects muons in the outer part of the detector.

Parton Particles (quarks and gluons) that make up hadrons.

Parton showering A cascade of partons produced by hard-scatter events.

PDF Parton distribution function.

Pile-up The phenomenon of multiple particle interactions occurring within one bunch crossing.

Pythia A Monte Carlo generator that simulates hadronization and parton showering.

QCD Quantum chromodynamics. The theory of strong interactions between quarks and gluons.

ROOT A program developed at CERN initially for data analysis in particle physics.

SM The Standard Model of particle physics.

SR Signal region. A region of data with selection cuts applied in order to isolate events of interest.

VEV Vacuum expectation value.

Chapter 1

Introduction

There is clear evidence for the existence of dark matter (DM), however its nature is unknown and DM particles have not been found to date. There are many searches ongoing to detect such particles, classified as either indirect detection, direct detection or production of DM. The ATLAS detector located at the Large Hadron Collider is a detector searching for DM particles in proton-proton collisions. If the data collected show no excess signal, then limits can be set on DM model parameters. The primary objective of this thesis is to reproduce such limits using a fast simulation of the ATLAS detector response and a simplified systematics treatment. These limits are compared to those obtained from the full ATLAS analysis with the complete list of systematics. The background distributions and their systematic uncertainties are obtained from the full analysis. A frequentist profile likelihood test is applied to the data in order to set upper limits on the signal strength.

The outline of this thesis is as follows:

- **Chapter 1** reviews the Standard Model of particle physics, the evidence for dark matter, as well as an overview of the methods currently being used to search for dark matter particles.
- **Chapter 2** describes the theory of the dark matter model of interest in this thesis in the context of a Mono-Z final state search; missing transverse momentum is defined, and the discriminant variable for the analysis is introduced.
- The fast simulation software for the ATLAS detector response is then described in **Chapter 3** and is validated through comparison with fully reconstructed samples.

- **Chapter 4** discusses the backgrounds and systematic uncertainties to the Mono-Z search.
- The statistical tests used for model parameter limit setting are discussed in **Chapter 5**.
- The results are presented in **Chapter 6**, followed by a conclusion in **Chapter 7**.

1.1 Standard Model of particle physics

The Standard Model (SM) describes all of the elementary particle interactions measured to date, in a framework including the three generations of fermions which compose the known matter of the universe and their anti-matter counterpart, as well as scalar and vector bosons which carry the forces that cause the particles to interact with each other.

Fermions obey Fermi-Dirac statistics, have $\frac{1}{2}$-integer spin, and hence obey the Pauli exclusion principle. Bosons obey Bose-Einstein statistics and have integer spin. Fermions are divided into two types, quarks and leptons, and their corresponding anti-particle.

Type	Particle	Mass	q
Quark	Up (u)	$2.16^{+0.49}_{-0.26}$ MeV	$+\frac{2}{3}$
	Charm (c)	1.27 ± 0.02 GeV	
	Top (t)	172.76 ± 0.30 GeV	
	Down (d)	$4.67^{+0.48}_{-0.17}$ MeV	$-\frac{1}{3}$
	Strange (s)	93^{+11}_{-5} MeV	
	Bottom (b)	$4.18^{+0.03}_{-0.02}$ GeV	
Lepton	Electron (e)	$0.5109989461 \pm 0.0000000031$ MeV	-1
	Muon (μ)	$105.6583745 \pm 0.0000024$ MeV	
	Tau (τ)	1776.86 ± 0.12 MeV	
Neutrino	ν_e	$m < 1.1$ eV	0
	ν_μ		
	ν_τ		

Table 1.1: Fermions of the Standard Model of particle physics [1]. q corresponds to the electric charge.

There are six types of quarks within three generations of weak doublets. They carry color charge, and as a result interact via the strong interaction as well as the weak and electromagnetic forces. Quarks combine to create hadrons, but cannot exist by themselves outside of a color singlet hadronic state.[1]

Similarily, there are six types of leptons, which are also classified into three lepton generations. Leptons only interact via the weak and electromagnetic forces, however the neutral leptons, the electron, μ and τ neutrinos, only interact via the weak force. The neutrinos are also assumed to be massless in the SM; however, neutrino oscillations have been measured which indicate that neutrinos have mass. The lepton and quark masses, as well as their electric charge, can be found in Table 1.1.

Type	Particle	Mass	Electric Charge
Gauge boson	Photon (γ)	0	0
	Gluon (g)		
	Z boson	91.1876 ± 0.0021 GeV	
	$W^{\pm}$ boson	80.379 ± 0.012 GeV	±1
Scalar boson	Higgs boson (H^0)	125.10 ± 0.14 GeV	0

Table 1.2: Bosons of the Standard Model of particle physics [1].

Four types of vector bosons are included in the model, that are exchanged between fermions and cause the interactions between them. Eight gluons mediate the strong force between quarks, the photon mediates the electromagnetic force between charged particles, and the $Z/W^{\pm}$ mediates the weak force. The only known fundamental force not included in the Standard Model is gravity. The Higgs boson, discovered in 2012 [2] [3], is the only known fundamental scalar boson and is a byproduct of the Higgs mechanism responsible in giving SM elementary particles their mass [4]. The boson masses and their electric charges can be found in Table 1.2.

Feynman diagrams are used to represent particle interactions at a given order in perturbation theory and are a pictoral way of representing probability amplitudes of quantum processes. Examples of Feynman diagrams can be found in Figure 1.1. Quantum electrodynamics and quantum chromodynamics each have their own set of rules for computing probabilty amplitudes using Feynman diagrams. More information about Feynman rules can be found in [7] and [8].

[1] Quarks and gluons are able to exist in an unconfined state, but only at very high temperatures, as a quark-gluon plasma.

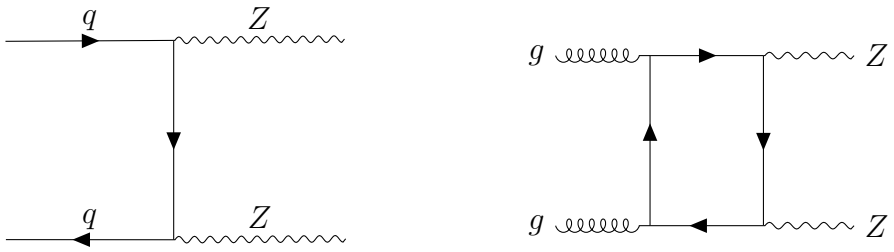

Figure 1.1: Example lowest-order and next-to-lowest-order Feynman diagrams for ZZ production. Here, the initial states are on the left of the diagrams and the final states are on the right [5] [6].

1.2 Evidence for dark matter

The Standard Model accounts for all particle physics processes measured to date. However, it does not explain the nature of dark matter, which is one reason for the need for Beyond the Standard Model (BSM) theories. The following sections describe important astronomical evidence for the existence of dark matter.

1.2.1 Galaxy rotation curves

Rotation curves of galaxies are assumed by Keplerian physics to fall off as a function of $\frac{1}{\sqrt{r}}$, where r is the radial distance from the centre of the galaxy, as the mass density is expected to reduce away from the galactic center. However, this is not the case as observed in most galaxies: the outer visible stars have a rotation speed almost as large, or larger than the ones near the center of the galaxy (see Figure 1.2) [9]. This suggests the existence of extra mass in the shape of a halo surrounding the galaxy, giving the outer material its high velocity.

1.2.2 Gravitational lensing

Gravitational lensing occurs when an object, such as a galaxy or cluster of galaxies, is so massive that due to general relativity, it can bend the light coming from behind it (see Figure 1.3). The level of bending that occurs for an object can be calculated given its mass, however in many instances, the observed gravitational lensing is more than expected. This suggests there is extra mass, assumed to be DM. Gravitational lensing allows the measurement of DM mass distributions between galaxies and galaxy clusters.

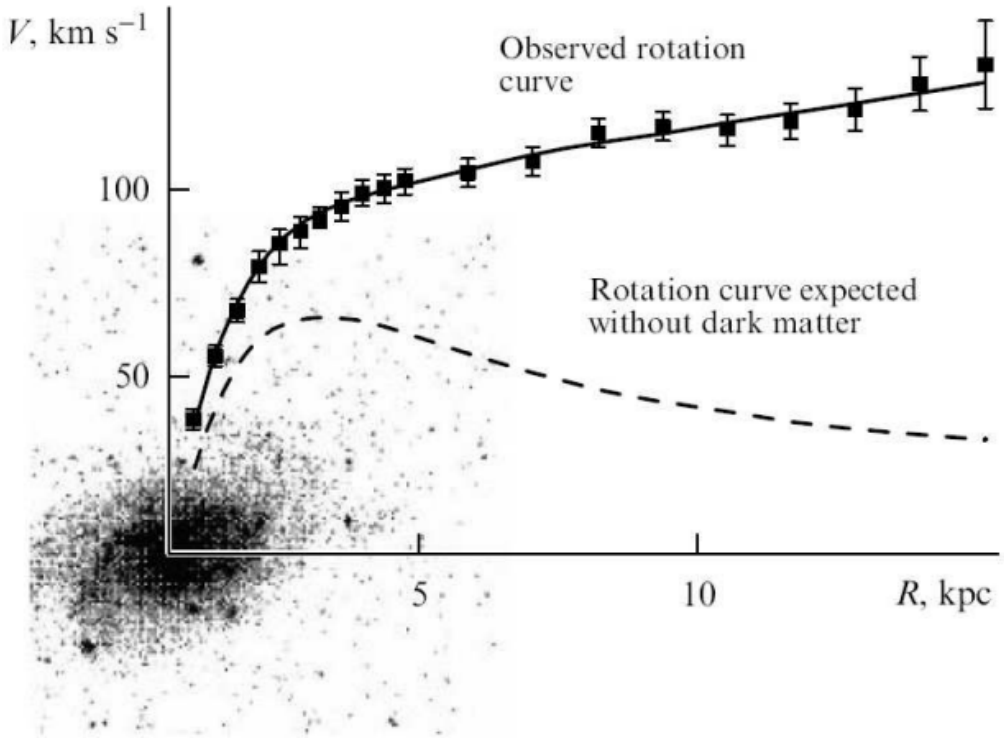

Figure 1.2: Observed rotation curve of the M 33 galaxy and the expected rotation curve without the existence of dark matter [9].

1.2.3 Bullet Cluster

The Bullet Cluster consists of the collision of two clusters of galaxies. If the universe consisted only of baryonic matter, the majority of the mass would be found where the hot gas is shown in pink in Figure 1.4. However, using gravitational lensing, it was found that the vast majority of the mass is located outside of this hot gas, shown in blue in two separate areas [11]. This is evidence that DM weakly interacts with baryonic matter, as the DM is able to travel through the clusters' collision undisturbed. [12].

1.3 Dark matter particle detection methods

The methods currently used to search for dark matter particles are direct detection, indirect detection, and production of DM particles in colliders. Indirect detection experiments of DM, for example the Fermi γ-ray Space Telescope [14], consist of analyzing astrophysical measurements of high energy process byproducts that

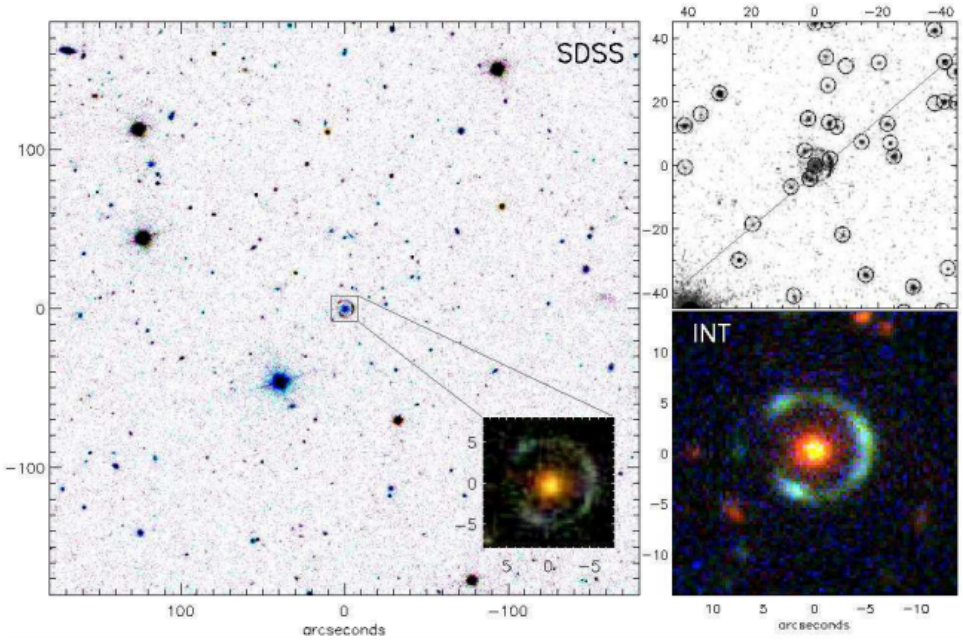

Figure 1.3: Sloan Digital Sky Survey (SDSS) spectral view of the Cosmic Horshoe. Gravitiational lensing can be seen in blue around the massive red object [10].

cannot be explained by baryonic matter alone. Direct detection experiments, such as XENON1T [15], involve experimentally measuring DM's collision effects on baryonic matter. Production of DM is attempted through high energy collisions, such as at the Large Hadron Collider [16]. So far, no experimental evidence has been found for the existence of DM particles.

1.3.1 Dark matter production

The Large Hadron Collider (LHC), a 27 km circumference collider located in Geneva, Switzerland, uses proton-proton collisions to study both SM and BSM physics. The most recent results are from Run II, which took place from 2015-2018 at a center of mass energy of 13 TeV with a peak luminosity of 1.74×10^{34} cm^{-2}s^{-1} [18]. So far, the LHC has collected 140 fb^{-1} of data. Run III is to start in 2022 at 13 TeV, with the goal of reaching 14 TeV. Although a DM particle has not yet been detected, the collected data can be used to set limits on DM model parameters. Since produced DM particles are expected not to be directly detected, missing transverse momentum, which will be introduced in Chapter 2, is generally the quantity of interest.

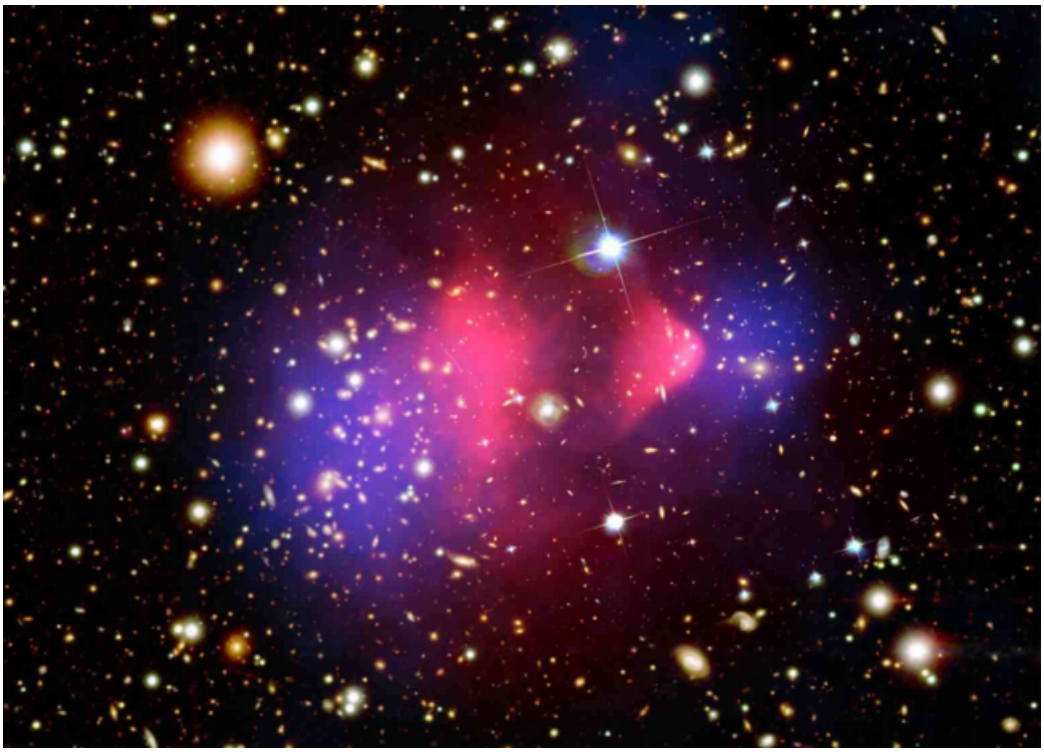

Figure 1.4: Galaxy Cluster 1E0657-56: The Bullet Cluster. The x-rays from hot baryonic matter and gas is shown in pink, while the mass distribution obtained from gravitational lensing is shown in blue, in two separate areas [13].

1.3.2 The ATLAS detector

The ATLAS detector (**A** **T**oroidal **L**HC **A**pparatu**S**) is a multipurpose cylindrical detector located at the LHC. It has nearly 4π solid angle coverage, save for near the beam pipe. It is composed of four main parts, which are the inner detector (ID), the calorimeter, the muon spectrometer (MS) and the magnet system.

The ID performs the initial measurements for any charged particles that are a product of the collisions, including reconstructing particle tracks and measuring their momentum [19]. It is in a 2 T solenoidal magnetic field [20]. There are three types of trackers within the ID; the Pixel Detector, the Semi-Conductor Tracker (SCT), and the Transition Radiation Tracker (TRT) [21] [22]. The layout of these trackers, along with the solenoid magnet system, are at the centre of Figure 1.6. The Pixel Detector is the innermost part of the ID, consisting of cylindrical silicon pixel layers, followed by the silicon microstrips of the SCT [23]. The outer layer of the ID is the TRT, made of 4 mm drift tubes filled with a xenon gas mixture [23].

The calorimeter system, located just outside of the ID, consists of electromagnetic

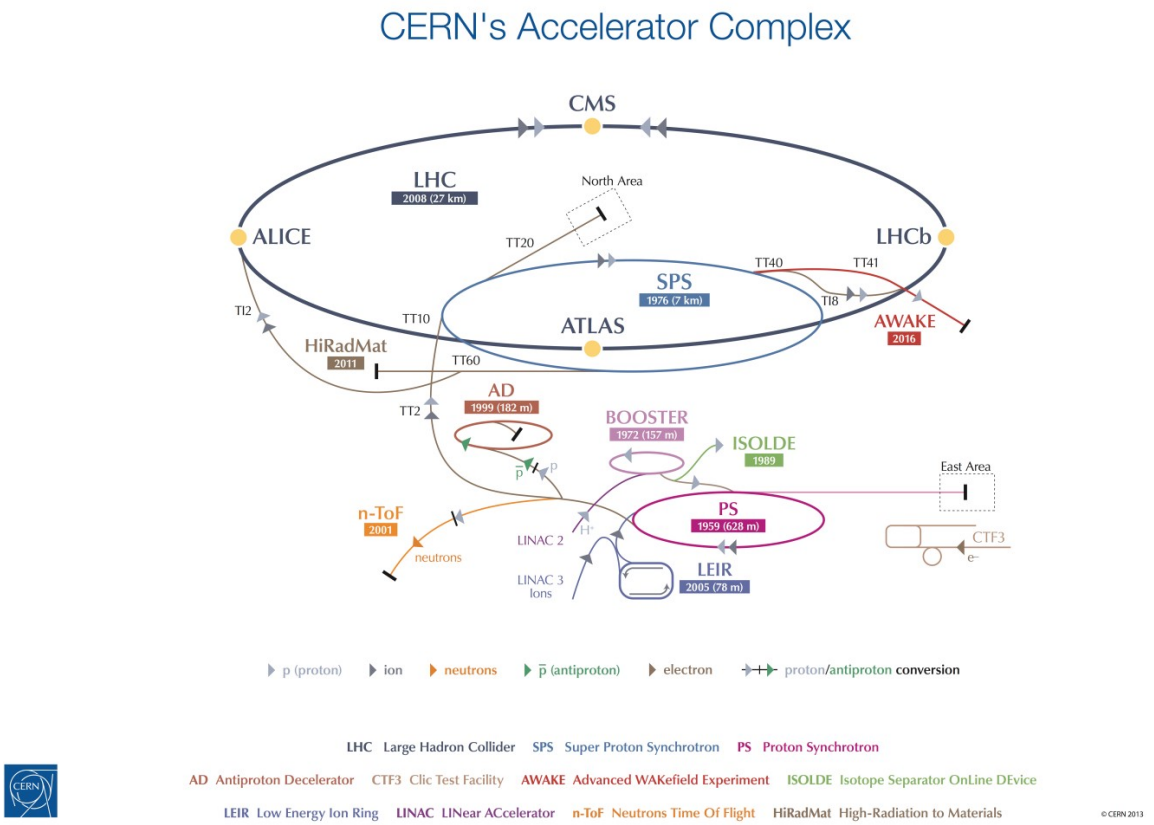

Figure 1.5: CERN's accelerator complex. The Large Hadron Collider is shown as an ellipse with a dark grey outline, while the main LHC detectors are shown as yellow circles surrounding its perimeter [17].

and hadronic calorimeters which detect and measure the energy of particle showers. It is composed of two types of detectors: the scintillating tile calorimeter and the liquid argon (LAr) calorimeter, both of which are sampling calorimeters. The tile calorimeter is the hadronic barrel calorimeter, and is composed of scintillators and steel [24]. The LAr calorimeter consists of the electromagnetic barrel calorimeter as well as the electromagnetic, hadronic and forward calorimeters located in each of the end-cap cryostats [25], which can be seen in Figure 1.6.

The MS is the outermost system, and is designed to detect muons in conjunction with the ID measurements, and in some events, the calorimeter measurements. It determines muon momenta by measuring the curvature of the trajectory of the particle caused by a toroidal magnet system [26]. Monitored drift tubes and cathode strip chambers are used for tracking muons, while resistive plate chambers and thin

gap chambers are implemented for triggering purposes in the barrel and end-cap, respectively [27]. The muon detectors and three toroidal magnets can be seen in the end-caps and barrel in Figure 1.6.

ATLAS utilizes a two-level trigger system in order to determine which events are to be recorded [28]. The Level-1 trigger is based on the information recorded by the calorimeter and muon spectrometer and makes decisions whether to keep event data or not within 2.5 μs [18]. The data kept are read by Read-Out Drivers and sent to the Data Acquisition System (DAQ). The DAQ then transports these events to the high level trigger to make the final decision on which events to keep. The final data sets are then processed and distributed to analysts around the world.

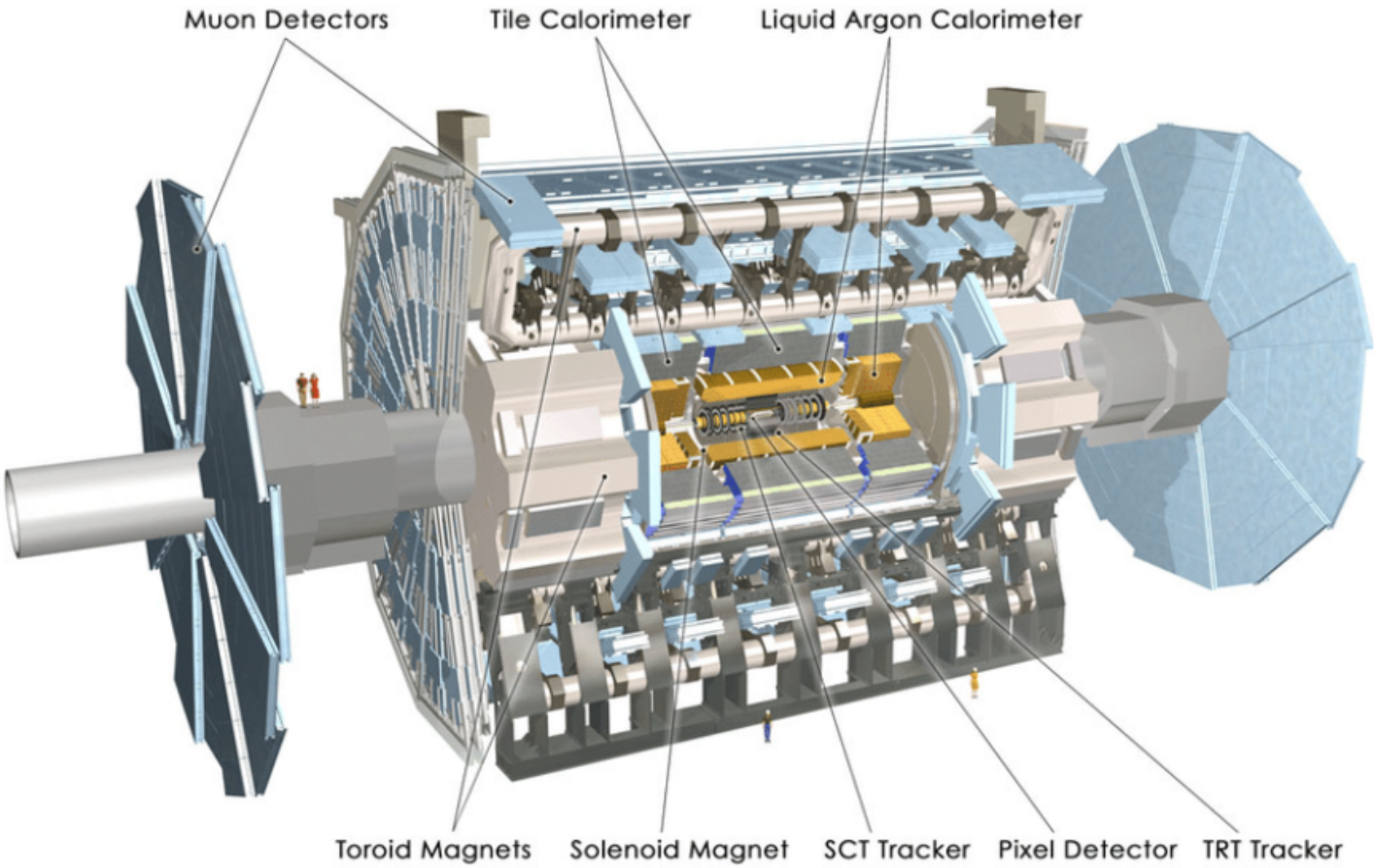

Figure 1.6: An overview of the ATLAS detector [29].

Chapter 2

Dark matter model with Mono-Z signature

The dark matter model studied in this thesis has a Mono-Z signature, where the final state is a leptonically decaying Z boson and a DM particle-antiparticle pair. While the DM particles cannot be directly detected, its presence can be inferred through a quantity called the missing transverse momentum.

2.1 Mono-Z

Commonly studied signatures that give a final state including a DM pair $\overline{\chi}\chi$ are the Mono-X signatures. Some examples include Mono-jet [30] and Mono-Higgs [31]. This analysis focuses on the Type II Mono-Z model, where the Z boson decays to two same-flavour leptons, either e^+e^- or $\mu^+\mu^-$.[1]

Two models were identified as benchmark models to probe the Mono-Z signature at the LHC: the simplified model, with a spin-1 vector or axial-vector mediator, and the two Higgs doublet model with an extra pseudoscalar (2HDMa); the focus of this thesis is on the 2HDMa model.

2.1.1 Simplified model

The vector/axial-vector simplified model has six free parameters: g_q the quark coupling constant, g_l the lepton coupling constant (here set to 0 for leptophobic model), g_χ the dark matter coupling constant, the mass m_χ of the dark matter particle, the mass m_{med} of the mediator, and Γ_{med} the mediator decay width [32] [33].

[1] Decay to two τ particles is kinematically allowed, but is unlikely to lead to a final state with an ee or $\mu\mu$ pair with both leptons satisfying the p_T selection, and with an invariant mass close to the Z mass. Hence, this decay has a negligible impact on the analysis.

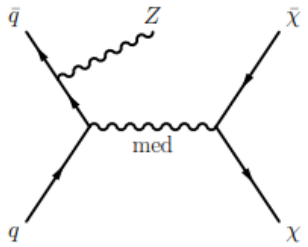

Figure 2.1: s-channel Feynman diagram for simplified dark matter model [20].

The simplified model assumes a dark matter pair coupling to a boson mediator (Z') to quarks via s-channel exchange (see Figure 2.1). Exclusion limits for the masses included in the model have been obtained by fixing the couplings to $g_q = 0.25$, $g_l = 0$, and $g_\chi = 1.0$ [20].

2.1.2 2HDMa

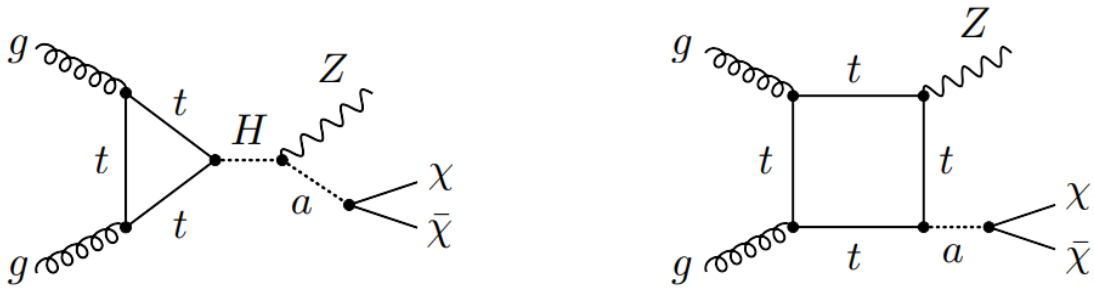

Figure 2.2: Example of Feynman diagrams for the two-Higgs doublet dark matter model with dark matter production via gluon fusion [34].

The 2HDMa model considered has five free parameters: the mass m_A of the heavy pseudoscalar, the mass m_a of the pseudoscalar mediator, the mass m_χ of the dark matter particle, $\sin\theta$, with the mixing angle θ defining the A and a particle, and $\tan\beta$, the ratio of the vacuum expectation values of the Higgs doublets. Four heavy Higgs particles are present in this model, and are set to $m_H = m_{H\pm} = m_A$. The heavy scalar Higgs is a necessary consequence of the model, and it can only decay to Standard Model fermions (or to aa/aZ final states) at first order. Assuming the heavy pseudoscalar A is sufficiently heavy (by setting its mass to $m_A = m_H$), it is kinematically allowed to decay to a $\chi\overline{\chi}$ pair, a fermion pair, or the ah final state [34].

It is also assumed to be a leptophobic model, so that the dark matter particles cannot couple to leptons. If the model were not sufficiently leptophobic, dark matter would be able to produce pairs of leptons by annihilation, giving an excess of ee or $\mu\mu$ pairs, which has been excluded by experiment.

The Lagrangian for the Yukawa couplings (coupling of the Higgs field to quark and lepton fields) is given by [34]

$$\mathcal{L}_Y = -\sum_{i=1,2} (\overline{Q} Y_u^i \tilde{H}_i u_R + \overline{Q} Y_d^i H_i d_R + \overline{L} Y_l^i H_i \ell_R + \text{h.c.}) \tag{2.1}$$

where Q and L are left-handed quark and lepton doublets, respectively, u_R and d_R are right-handed up and down quarks, and ℓ_R are right-handed leptons. For Type II dark matter, the Yukawa matrices are restricted to [34]

$$Y_u^1 = Y_d^2 = Y_l^2 = 0 \tag{2.2}$$

where Y_u^i, Y_d^i, Y_l^i are the Yukawa matrices acting on up quarks, down quarks and lepton singlets, respectively.[2] The Lagrangian for the dark matter χ coupling to the mediator a can be expressed as [35]

$$\mathcal{L}_\chi = g_\chi (\cos\theta a + \sin\theta A) \overline{\chi} i\gamma^5 \chi. \tag{2.3}$$

The vacuum expectation values (VEV) of the Higgs doublets present in the model are given by [34]

$$\langle H_i \rangle \;=\; (0, v_i/\sqrt{2})^T \tag{2.4}$$

where i is the index of the Higgs doublet, and the VEV of the SM Higgs field is [34]

$$v \;=\; \sqrt{v_1^2 + v_2^2} \simeq 246 \text{ GeV}. \tag{2.5}$$

We can then define the parameter $\tan\beta$, the ratio of the doublets' VEV, as [36]

$$\tan\beta = \frac{v_2}{v_1}. \tag{2.6}$$

[2] This implies that the up- and down-type quarks couple to different Higgs doublets, with leptons coupling to the same doublet as the down-type quarks.

The 2HDMa model can have either gg- or bb-induced production, with the gg-induced production dominating at low tanβ values. The models considered in this thesis have a tanβ value of 1.0, such that the dominant production mode is via gluon fusion.

The partial width for pseudoscalar mediator a to decay into a dark matter/anti-dark matter pair is [34]

$$\Gamma(a \to \chi\overline{\chi}) \quad = \quad \frac{g_\chi^2}{8\pi} M_a \beta_{\chi/a} \cos^2\theta \tag{2.7}$$

where $\beta_{\chi/a} = \sqrt{1 - 4m_\chi^2/M_a^2}$ is the velocity of particle χ. Due to the model's requirement that a be light, it can only decay to either dark matter or SM fermions at leading order due to its couplings (ahZ vertex, where h is the SM Higgs boson).

2.2 Missing transverse momentum

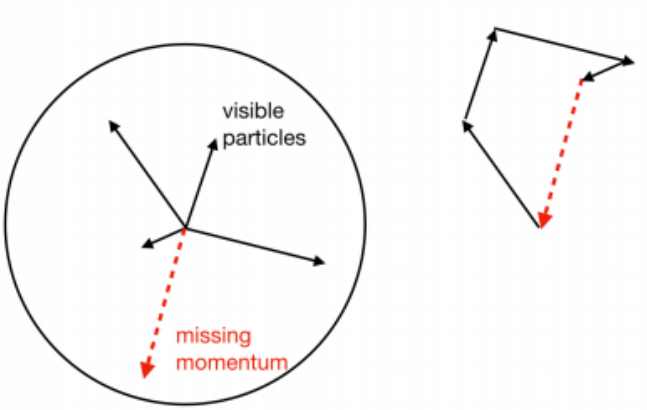

Figure 2.3: Diagram depicting the momentum vectors of particles in the transverse plane, as well as the vectorial sum of their momenta. If the sum of the momenta is not zero, the resultant momentum, depicted as the red arrow, is referred to as the missing transverse momentum of the event [37].

In principle, the total momentum perpendicular to the beam axis in particle collider final states should add to zero by conservation of momentum [38]. Certain processes that occur in the collider environment give weakly-interacting or undetected particles in the final state, giving the illusion of the violation of momentum conservation. This is referred to as missing transverse momentum, denoted here as $\vec{\not{E}}_T$, which

is an important observable for the detection of otherwise undetectable particles, such as neutrinos or dark matter.

Another important quantity related to transverse momentum is H_T, the sum of all scalar transverse momenta of reconstructed leptons, photons and jets. The magnitude of the missing transverse momentum $\not{E}_T$, is called the missing transverse energy [39]. In terms of reconstructed objects, $\vec{\not{E}}_T$ and H_T are then given by [39]

$$\vec{\not{E}}_T = -\left(\sum_{\text{leptons}} \vec{p_T} + \sum_{\text{photons}} \vec{p_T} + \sum_{\text{jets}} \vec{p_T} + \sum_{\text{soft}} \vec{p_T}\right) \tag{2.8}$$

$$H_T = \sum_{\text{leptons}} |\vec{p_T}| + \sum_{\text{photons}} |\vec{p_T}| + \sum_{\text{jets}} |\vec{p_T}| + \sum_{\text{soft}} |\vec{p_T}| \tag{2.9}$$

where $\vec{p_T}$ is the transverse momentum vector of each particle.[3] If the missing transverse energy of an event is significantly beyond the prediction of the SM, then that is evidence of physics beyond the SM. Thus, a precise reconstruction of $\not{E}_T$ is necessary for the discovery of new physics.

The maximum $\not{E}_T$ for the Mono-Z final state in the limit of heavy Higgs mass $M_H > M_a + M_Z$ is given as [34]

$$\not{E}_T^{\max} \simeq \frac{\lambda^{1/2}(M_H, M_a, M_Z)}{2M_H} \tag{2.10}$$

where $\lambda(m_1, m_2, m_3) = (m_1^2 - m_2^2 - m_3^2)^2 - 4m_2^2 m_3^2$.

2.3 Backgrounds and event selection

Many backgrounds exist that may produce the Mono-Z signature. To reduce these backgrounds, predetermined selection cuts are made on the data, defining the signal region (see Table 2.1). The main background present is ZZ, where one Z decays to two leptons, and the other decays to neutrinos that are invisible to the detector, resulting in a significant measure of $\not{E}_T$. The ZZ background accounts for the majority (59%) of the background and is irreducible. Its contribution to the total background is estimated by simulation, since the data sample of ZZ is statistically limited. The other important backgrounds include WZ (25%, also estimated by simulation), Z+jets (8%, estimated by data and by simulation), and non-resonant (8%)

[3] Leptons, photons and jets are considered 'hard' reconstructed objects, while 'soft' reconstructed tracks are not associated with a specific particle.

Selection criteria	Background Reduced
Opposite-sign leptons, leading (subleading) $p_T > 30$ (20) GeV	–
Third lepton veto	WZ
$\lvert\eta_e\rvert < 2.47$, $\lvert\eta_\mu\rvert < 2.50$	–
$76 < m_{ll} < 106$ GeV	Non-resonant
$\not{E}_T > 90$ GeV	Z+jets
$\Delta R_{ll} < 1.8$	Z+jets, Non-resonant
$\not{E}_T/\sqrt{H_T} > c$	Z+jets

Table 2.1: Selection critera applied to generated events, where c is a sample-dependant value [41].

backgrounds, such as $t\bar{t}$, Wt, and WW.

The less important backgrounds include W+jets, VVV, and $t\bar{t}V(V)$,[4] some of which are not included in this analysis, as their contribution to the total background is negligeable [20].

The selection criteria requires events with one lepton pair with the same flavour, ee or $\mu\mu$, opposite charge, and sufficient transverse momentum p_T. The leading lepton must have a p_T greater than 30 GeV, and the subleading lepton a p_T greater than 20 GeV. Events with a third lepton with $p_T > 7$ GeV are removed, which reduces the second largest background, WZ. The total mass of the lepton pair must be in the Z mass window $76 < m_Z < 106$ GeV, which reduces WW background. The pseudorapidity, defined in terms the angle of a particle with respect to the beam axis, is given as [40]

$$\eta = -\ln\left(\tan\left(\frac{\theta}{2}\right)\right) \tag{2.11}$$

and is required to be $|\eta| < 2.47$ for electrons and $|\eta| < 2.50$ for muons. In order to reduce the Z+jets background, which occurs from mismeasurements of jets that produce fake $\not{E}_T$, it is required that $\not{E}_T$ must be greater than 90 GeV. The separation between the two leptons, ΔR, must be less than 1.8, and is defined as $\Delta R = \sqrt{(\Delta\phi)^2 + (\Delta\eta)^2}$, where $\Delta\eta$ is the pseudorapidity separation and $\Delta\phi$ the azimuthal separation angle. $\not{E}_T/\sqrt{H_T}$ must be greater than a predetermined constant c, which is sample-dependant, in order to require a significant $\not{E}_T$. More information on $\not{E}_T/\sqrt{H_T}$ can be found in Section 3.2.1.

[4] Here, V is the W or Z vector boson.

2.4 m_{TZZ} as event discriminant

The event discriminant for the Mono-Z analysis is the ZZ transverse mass. We can define the transverse mass of a two particle system as [1]

$$m_T^2 = (E_{T,1} + E_{T,2})^2 - (\vec{p}_{T,1} + \vec{p}_{T,2})^2 \tag{2.12}$$

where

$$E_{T,i}^2 = m_i^2 + \vec{p}_{T,i}^{\,2} \tag{2.13}$$

is called the transverse energy for particle i, and m_i is the mass of the particle. Inserting this into the definition, 2.12 becomes

$$m_T^2 = \left(\sqrt{m_1^2 + |\vec{p}_{T,1}|^2} + \sqrt{m_2^2 + |\vec{p}_{T,2}|^2}\right)^2 - (\vec{p}_{T,1} + \vec{p}_{T,2})^2. \tag{2.14}$$

The analysis strategy for a Mono-Z search is virtually identical to that for the search of ZZ resonance with one invisible Z, such that the variable m_{TZZ} can be used as the discriminant for Mono-Z searches. For a system with two Z bosons, let $E_{T,1}$ be the transverse energy of the leptonically-decaying Z boson and $E_{T,2}$ be the invisibly decaying Z. Then by fixing m_1 and m_2 to the mass of the Z boson as per [1],

$$E_{T,1}^2 = m_Z^2 + |\vec{p}_T^{\,\ell\ell}|^2 \tag{2.15}$$

$$E_{T,2}^2 = m_Z^2 + |\vec{\not{E}}_T|^2. \tag{2.16}$$

The transverse mass for the ZZ system becomes

$$m_{TZZ}^2 = \left(\sqrt{m_Z^2 + |\vec{p}_T^{\,\ell\ell}|^2} + \sqrt{m_Z^2 + |\vec{\not{E}}_T|^2}\right)^2 - \left|\vec{p}_T^{\,\ell\ell} + \vec{\not{E}}_T\right|^2 \tag{2.17}$$

where $\vec{p_T}^{\,\ell\ell}$ is the transverse momentum of the lepton pair. This variable definition is the event discriminant for the Mono-Z dark matter search. By definition, it is invariant under longitudinal boosts. But, unlike $\not{E}_T$, it is weakly dependent on the ZZ system transverse boost, which makes it less sensitive to mismodelling of the $Z\chi\overline{\chi}$ system transverse momentum.

Chapter 3

Signal event generation and reconstruction

The final objective of this analysis is to assess the use of a fast detector simulation software in reproducing the official ATLAS m_{TZZ} signal distributions and to explore the effect of simplifying the systematic error treatment. To this end, 2HDMa signal events with a $Z(\ell^+\ell^-) + \chi\overline{\chi}$ final state are generated by MadGraph, the generator used for hard scattering events [42]. Pythia is then applied over the events to simulate hadronization and parton showering [43]. Once this is completed, Delphes is run over the signal samples to simulate the ATLAS detector response [44] [45].

3.1 Delphes software

Delphes is a fast simulation software for cylindrical detectors such as CMS and ATLAS that consist of an inner detector, calorimeters, muon spectrometer and magnet system [45]. It is used for developing strategies for the analysis of data obtained by these detectors.

The treatment of particle reconstruction is as follows, from [45]. Particles created within the ID travel until they reach a calorimeter, and particles created outside the ID are disregarded. Neutral particles are simulated to follow a trajectory unaltered by the magnet system until they reach a hadronic calorimeter (HCAL) cell. Charged particles are affected by the magnetic field and follow a helicoidal path until they reach an electromagnetic calorimeter (ECAL) cell. ECAL and HCAL cells are assumed to be perfectly pointing to the vertex, making a tower cell. The energy deposited into a tower by a particle depends on the assumed ECAL and HCAL resolutions. Particles such as muons and neutrinos do not interact with the calorimeters.

Delphes computes the particle energies using their momentum and the detector

sinθ	σ (fb)
0.1	1.0002 ± 0.0006
0.2	3.7410 ± 0.0060
0.3	7.5824 ± 0.0044
0.4	11.881 ± 0.021
0.5	16.062 ± 0.021
0.6	19.883 ± 0.019
0.7	23.159 ± 0.025
0.9	28.142 ± 0.024

Table 3.1: Cross sections of the gg-induced sinθ scan samples, generated with tanβ = 1.0, m_H = 600 GeV, m_a = 200 GeV and m_{DM} = 10 GeV.

energy resolution. The simulated detector energy resolution is given by

$$\left(\frac{\sigma}{E}\right)^2 = \left(\frac{S(\eta)}{\sqrt{E}}\right)^2 + \left(\frac{N(\eta)}{E}\right)^2 + C(\eta)^2 \tag{3.1}$$

where S, N, C are stochastic, noise and constant terms, respectively. The ECAL and tracker resolution are used to compute the electron energy resolution, with the tracker resolution dominating at low energy. In DELPHES 3, there is no electron or muon fake rate implemented in the software; photons as well as electrons with no track are both reconstructed as photons, which are also reconstructed using the ECAL. The treatment of pile-up and the reconstruction of individual hard objects allows the calculation of the missing transverse momentum used in this analysis.

3.2 Signal generation using MadGraph and Delphes

Several $pp \to Z(\ell^+\ell^-) + \chi\overline{\chi}$ signal samples are generated for various values of sinθ, with tanβ = 1.0, $m_H = m_A$ = 600 GeV, m_a = 200 GeV and m_χ = 10 GeV. The sinθ values and the corresponding cross sections can be found in Table 3.1. The samples are generated with 100 000 events using MADGRAPH5_AMC@NLO to produce the hard scatter events and PYTHIA 8 for the hadronization and parton showering. DELPHES 3 is applied over the generated samples in HepMC formatted files to simulate the ATLAS detector response. The resulting ROOT file is used as input for the analysis step, which applies object and event selection and creates kinematic distributions to be used for validation purposes and finally as input into HISTFITTER for obtaining signal strength limits (see Chapter 5).

The default DELPHES settings for the ATLAS detector performance were in part taken from test beam results. DELPHES is applied using its default ATLAS parameters, with the following changes:

- the $\vec{\not{E}}_T$ calculation is altered to be based on jets, electrons, muons and photons (the default calculation considers calorimeter-based EFlow objects merged with all tracks);
- the minimum transverse momentum for jets is changed from 20 GeV to 30 GeV for Jet Finder and Jet Pile-Up Subtraction;
- the angular separation ΔR is changed from 0.6 to 0.4 for MC Truth Jet Finder and Jet Finder.

The changes made to the DELPHES parameter card used are listed in Appendix A.

3.2.1 $\not{E}_T$ significance substitution

$\not{E}_T$ significance is a measure of how much the observed $\not{E}_T$ differs from the one expected from detector resolution and inefficiencies. A significant $\not{E}_T$ implies that particles invisible to the detector such as neutrinos or dark matter are the likely cause for the excess transverse momentum. Event-based $\not{E}_T$ significance is defined as [39]

$$\mathcal{S} = \frac{\not{E}_T}{\sqrt{H_T}} \tag{3.2}$$

and has been used in previous ATLAS analyses. Event-based $\not{E}_T$ significance is solely based on calorimeter signals, so a new object-based definition has been developed to take into account resolutions and mismeasurements for higher $\not{E}_T$ significance precision.

Object-based $\not{E}_T$ significance $\mathcal{S}$ is defined as [39]

$$\mathcal{S}^2 = 2\ln\left(\frac{\max_{p_T^{\text{inv}}\neq 0}\mathcal{L}(\not{E}_T|p_T^{\text{inv}})}{\max_{p_T^{\text{inv}}=0}\mathcal{L}(\not{E}_T|p_T^{\text{inv}})}\right) \tag{3.3}$$

where p_T^{inv} is the transverse momentum of particles invisible to the detector, and $\mathcal{L}(\not{E}_T|p_T^{\text{inv}})$ is the likelihood of p_T^{inv} given $\not{E}_T$. $\mathcal{S}$ is hence based on the ratio of the maximum likelihoods of the true $\not{E}_T$ hypothesis over that of the fake $\not{E}_T$ hypothesis.

DELPHES 3 does not have a defined $\not{E}_T$ significance object, therefore a $\not{E}_T$ significance cut cannot easily be applied to the generated events. In this thesis, $\not{E}_T/\sqrt{H_T}$ has been chosen as an appropriate substitute, due to the definition of event-based $\not{E}_T$ significance and its relation to the object-based definition.

The event selection cut for $\not{E}_T/\sqrt{H_T}$ is found as follows: first, the ratio of events before and after the $\not{E}_T$ significance cut in the fully reconstructed ATLAS sample is computed. Then, the value of $\not{E}_T/\sqrt{H_T}$ that gives the same ratio is found for the DELPHES samples. Events with $\not{E}_T/\sqrt{H_T}$ above that value are kept. The cut values are sample-dependent and can be found in Table 3.2. An example of the $\not{E}_T$ distribution before and after the cut can be found in Figure 3.1.

sinθ	$\not{E}_T/\sqrt{H_T}$ Cut	Eff % (D, ee)	Eff % (D, $\mu\mu$)	Eff % (A, ee)	Eff % (A, $\mu\mu$)
0.35*	9.15	0.838 ± 0.009	0.833 ± 0.007	0.835 ± 0.003	0.833 ± 0.003
0.7**	9.10	0.842 ± 0.008	0.826 ± 0.007	0.836 ± 0.002	0.831 ± 0.002
0.1	9.35	0.833 ± 0.009	0.823 ± 0.007	0.839 ± 0.003	0.832 ± 0.003
0.2	9.00	0.831 ± 0.009	0.839 ± 0.007	0.838 ± 0.003	0.832 ± 0.003
0.3	9.02	0.842 ± 0.009	0.830 ± 0.007	0.838 ± 0.003	0.832 ± 0.003
0.4	9.27	0.832 ± 0.009	0.838 ± 0.007	0.838 ± 0.002	0.832 ± 0.002
0.5	9.20	0.839 ± 0.008	0.831 ± 0.007	0.837 ± 0.002	0.831 ± 0.002
0.6	9.20	0.836 ± 0.009	0.833 ± 0.007	0.837 ± 0.002	0.831 ± 0.002
0.9	9.20	0.844 ± 0.009	0.821 ± 0.007	0.835 ± 0.003	0.831 ± 0.003

Table 3.2: $\not{E}_T/\sqrt{H_T}$ cut values applied to the DELPHES distributions. The efficiency for the ATLAS (A) samples were found by taking the ratio of the number of events kept after/before the $\not{E}_T$ significance cut. The efficiency for the DELPHES (D) samples were found by estimating the $\not{E}_T/\sqrt{H_T}$ value needed to get approximately the same efficiency as for the ATLAS sample. For the fully reconstructed ATLAS samples, sinθ = 0.35 is used as a validation sample, while sinθ = 0.7 is used as the base for MadGraph reweighting. All other listed fully reconstructed samples are reweighted from this point.

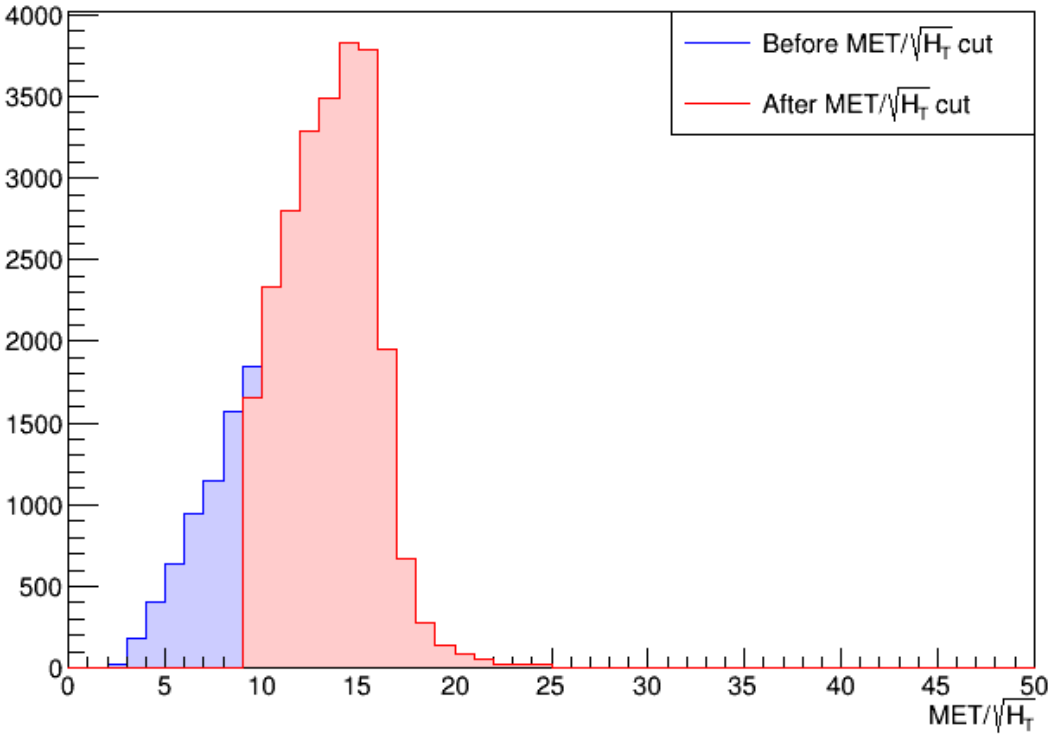

Figure 3.1: $\not{E}_T/\sqrt{H_T}$ (MET/$\sqrt{H_T}$) distributions before and after the designated cut value listed in Table 3.2 for $\mu\mu$ channel, gg-induced sample with $\tan\beta = 1.0$, $\sin\theta = 0.7$, $m_A = m_H = 600$ GeV, $m_a = 200$ GeV and $m_\chi = 10$ GeV. 82.7% of events are kept after the cut.

3.2.2 Acceptance

In order to properly normalize the DELPHES distributions, the acceptances for the samples must be calculated. The acceptance for the chosen samples is [46]

$$a = \epsilon \left(\frac{n}{N} \right) \tag{3.4}$$

and is in fact the acceptance times efficiency, where n is the sum of weights after all cuts, N is the sum of weights at AOD level, and ϵ is the filter efficiency, defined as

$$\epsilon = \frac{N}{M} \tag{3.5}$$

where M is the sum of weights at generator level. The square of the uncertainty of the acceptance is given as

$$\sigma_a^2 = \epsilon^2 \left[\frac{\sigma_n^2 (N-n)^2 + (\sigma_N^2 - \sigma_n^2) n^2}{N^4} \right] \tag{3.6}$$

for weighted events, where σ_n and σ_N are the uncertainties of n and N, respectively. For unweighted events, the uncertainty of the acceptance is given as

$$\sigma_a = \frac{\epsilon \sigma_n}{N} \sqrt{1 - \frac{n}{N}} \tag{3.7}$$

in the limit where the uncertainty in the filter efficiency goes to zero. The DELPHES signal events are unweighted, such that n is taken from the final cutflow step (after all cuts), and N is taken before any cuts are made.

The calculated acceptances for both the ATLAS and DELPHES distributions can be found in Table 3.3. As seen in this table, the acceptances for the ee channel for the DELPHES distributions are smaller than that for the ATLAS distributions. This is likely due to limitations in the DELPHES software, or in its configuration.

In an attempt to fix the electron acceptance, a few changes to the DELPHES parameter card were investigated. First, the electron isolation was turned off. This slightly improved the acceptance, however it skewed the $M_{\ell\ell}$ distribution and made it asymmetric about the Z mass peak, as there were many more events with low values for the invariant mass. Then, the photons were turned off completely. This fixed the acceptance, however it greatly skewed the $M_{\ell\ell}$ distributions. Finally, electron dressing was implemented, under the hypothesis that perhaps the Bremsstrahlung radiation

was not simulated properly. Only a handful of electrons were dressed, with minimal impact. Since these changes did not fix the acceptance problem, the changes were discarded. Improving this further was deemed beyond the scope of this work, and so the acceptances are therefore scaled in order to properly normalize the distributions to the ATLAS integrated luminosity of 139 fb^{-1}.

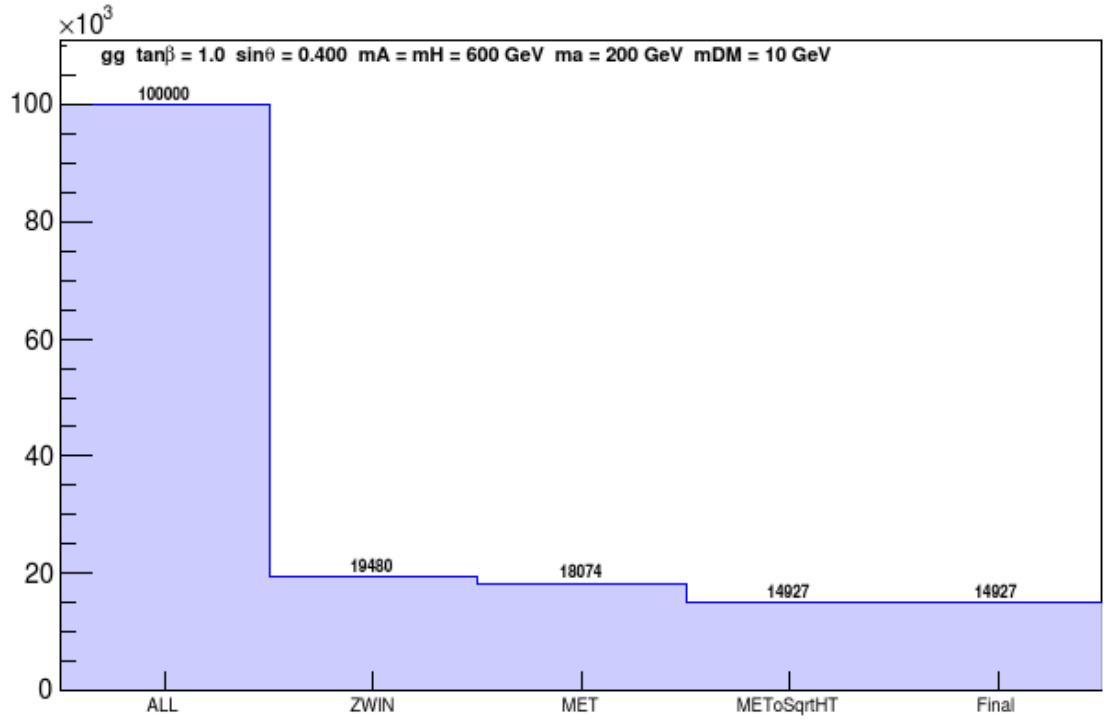

(a) ee channel cutflow.

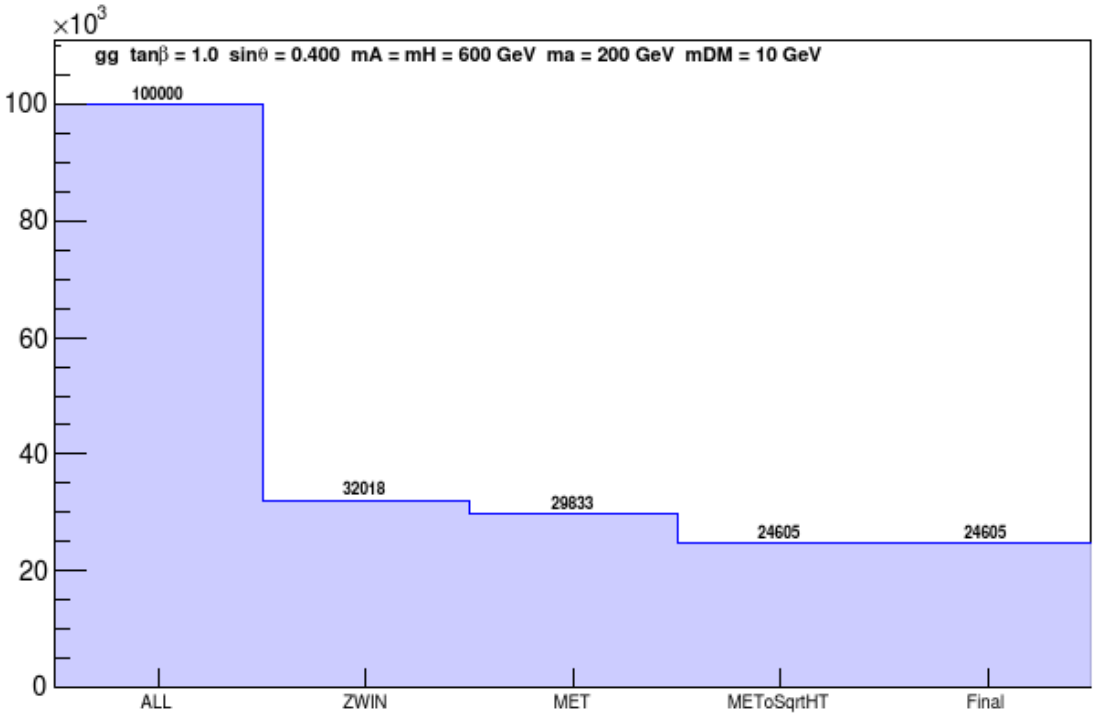

(b) $\mu\mu$ channel cutflow.

Figure 3.2: ee and $\mu\mu$ channel cutflows for $\sin\theta = 0.4$. To find the acceptance, n is taken from the Final cutflow step, and N is taken from the ALL cutflow step. ZWIN is the Z mass window cut, MET is the $\not{E}_T$ cut, and METoSqrtHT is the $\not{E}_T/\sqrt{H_T}$ cut, as defined in Table 2.1.

$\sin\theta$	ϵ	a (A, ee)	a (A, $\mu\mu$)	a (D, ee)	a (D, $\mu\mu$)	r_{ee}	$r_{\mu\mu}$
0.35*	0.9900	0.2503 ± 0.0052	0.2532 ± 0.0053	0.1454 ± 0.0023	0.2582 ± 0.0029	1.737 ± 0.045	0.9828 ± 0.0233
0.7**	0.9897	0.2509 ± 0.0072	0.2529 ± 0.0073	0.1496 ± 0.0011	0.2463 ± 0.0014	1.677 ± 0.050	1.027 ± 0.029
0.1	-	0.2534 ± 0.0025	0.2544 ± 0.0025	0.1503 ± 0.0030	0.2362 ± 0.0036	1.685 ± 0.038	1.077 ± 0.020
0.2	-	0.2534 ± 0.0025	0.2544 ± 0.0025	0.1503 ± 0.0011	0.2512 ± 0.0014	1.685 ± 0.021	1.012 ± 0.011
0.3	-	0.2534 ± 0.0025	0.2544 ± 0.0025	0.1528 ± 0.0017	0.2490 ± 0.0021	1.659 ± 0.025	1.022 ± 0.013
0.4	-	0.2534 ± 0.0025	0.2544 ± 0.0025	0.1493 ± 0.0011	0.2461 ± 0.0014	1.692 ± 0.021	1.031 ± 0.012
0.5	-	0.2534 ± 0.0025	0.2544 ± 0.0025	0.1477 ± 0.0021	0.2462 ± 0.0014	1.707 ± 0.030	1.030 ± 0.012
0.6	-	0.2534 ± 0.0025	0.2544 ± 0.0025	0.1468 ± 0.0022	0.2445 ± 0.0014	1.712 ± 0.031	1.035 ± 0.012
0.7	-	0.2534 ± 0.0025	0.2544 ± 0.0025	0.1496 ± 0.0011	0.2463 ± 0.0014	1.694 ± 0.021	1.033 ± 0.012
0.9	-	0.2534 ± 0.0025	0.2544 ± 0.0025	0.1451 ± 0.0020	0.2492 ± 0.0025	1.725 ± 0.029	1.013 ± 0.014

Table 3.3: Acceptances for ATLAS (A) and DELPHES (D) samples for ee and $\mu\mu$ channels, where ϵ is the filter efficiency (n/a for reweighted samples), along with their ratios (ATLAS/DELPHES), r_{ee} and $r_{\mu\mu}$. For the fully reconstructed ATLAS samples, $\sin\theta = 0.35$ is used as a validation sample, while $\sin\theta = 0.7$ is used as the base for MadGraph reweighting. All other listed fully reconstructed samples are reweighted from this point.

3.2.3 Normalization using acceptance

To find the overall scaling factor, h, to normalize the DELPHES distributions to the ATLAS distributions, first the number of events in the DELPHES distributions needs to be scaled to better match the acceptances of the ATLAS samples. The ratio of acceptances r is calculated by

$$r = \left\langle \frac{a_A}{a_D} \right\rangle \tag{3.8}$$

where a_A is the acceptance for the ATLAS samples, and a_D is the acceptance for the DELPHES samples. The ratios are found in the last two columns of Table 3.3. The average ratio is taken over all the sinθ samples, separately for the ee ($r_{ee} = 1.697$) and $\mu\mu$ ($r_{\mu\mu} = 1.026$) channels.

The DELPHES kinematic distributions in the final cutflow step need to be scaled by the ratio r as well as a factor k to account for the difference in luminosity. k is the luminosity ratio, given as

$$k = \frac{\mathcal{L}}{\mathcal{L}^{MC}} = \frac{\sigma\mathcal{L}}{N^D_{ALL}} \tag{3.9}$$

where $\mathcal{L} = 139\,\text{fb}^{-1}$ is the ATLAS integrated luminosity, $\mathcal{L}$ is the Monte Carlo effective integrated luminosity for the DELPHES samples, σ is the cross section associated with the sample and obtained from MADGRAPH, and

$$N^D_{ALL} = \sigma\mathcal{L}^{MC}. \tag{3.10}$$

The scaling factor can now be described as

$$\frac{\sigma\mathcal{L}}{N^D_{ALL}} r. \tag{3.11}$$

Once the DELPHES kinematic distributions are scaled in this way, they can be overlaid over fully reconstructed samples which are reconstructed using the full ATLAS software to validate the simulation method.

3.3 Comparison to fully reconstructed signal samples

The DELPHES kinematic distributions are overlaid onto the distributions obtained from the fully reconstructed samples, and their ratio is computed for each bin. The following metrics are calculated in order to obtain a quantitive comparison of the histograms bin by bin:

- χ^2/NDF, the χ^2 and number of degrees of freedom, where the degrees of freedom equals the number of bins in the histogram minus the number of bins with less than 10 effective number of events;
- $\langle|\epsilon|\rangle$, the average of the absolute value of the relative bin-by-bin difference between two histograms;
- δ_ϵ, the root mean square (rms) of the relative bin-by-bin difference between two histograms.

3.3.1 Histogram comparison metrics

Given a weighted histogram with total number of entries $N = \sum_{i=1}^{r} n_i$, where n_i is the number of entries for bin i, and another unweighted histogram with total number of entries $M = \sum_{i=1}^{r} m_i$, where m_i is the the number of entries for bin i, the χ^2 value is given by [47]

$$\chi^2 = \sum_{i=1}^{r} \frac{(n_i - N\hat{p}_i)^2}{N\hat{p}_i} + \sum_{i=1}^{r} \frac{(w_i - W\hat{p}_i)^2}{s_i^2} \tag{3.12}$$

where w_i is the weight of bin i for the weighted histogram, W is the sum of weights, $W\hat{p}_i$ is the expectation value for weight w_i, s_i^2 is the sum of squares of weights, and

$$\hat{p}_i = \frac{n_i + m_i}{N + M} \tag{3.13}$$

is the maximum likelihood estimator of p_i.

For two independent histograms, one with bin content a_j with error σ_{aj} and the other with bin content b_j with error σ_{bj} for bin j, the average of the relative difference

between the two histograms is given by [46]

$$\langle \epsilon \rangle = \frac{\sum_j \frac{\epsilon_j}{\sigma^2_{\epsilon j}}}{\sum_j \frac{1}{\sigma^2_{\epsilon j}}}, \qquad \text{where } \epsilon_j = \frac{b_j - a_j}{s_j}, \text{ and} \tag{3.14}$$

$$s_j = \frac{\frac{a_j}{\sigma^2_{aj}} + \frac{b_j}{\sigma^2_{bj}}}{\frac{1}{\sigma^2_{aj}} + \frac{1}{\sigma^2_{bj}}} \tag{3.15}$$

is the maximum likelihood estimate of the true bin content. The average of the absolute of the relative difference is then given by

$$\langle |\epsilon| \rangle = \frac{\sum_j \frac{|\epsilon_j|}{\sigma^2_{\epsilon j}}}{\sum_j \frac{1}{\sigma^2_{\epsilon j}}}. \tag{3.16}$$

The square of the rms of the relative difference is then

$$\delta^2_\epsilon = \langle \epsilon^2 \rangle = \frac{\sum_j \frac{\epsilon j^2}{\sigma^2_{\epsilon j}}}{\sum_j \frac{1}{\sigma^2_{\epsilon j}}}. \tag{3.17}$$

The full derivation for $\langle |\epsilon| \rangle$ and δ_ϵ can be found in Appendix B.

The χ^2/NDF, δ_ϵ, $\langle |\epsilon| \rangle$ and total content ratio values for different kinematic distributions for a fixed value of sinθ are listed in Tables 3.4 and 3.5, while the values for the m_{TZZ} distributions for the various sinθ values can be found in Tables 3.6 and 3.7. Smaller values of $\langle |\epsilon| \rangle$ and δ_ϵ indicate better shape agreement between the distributions, as it means that overall, there is a smaller difference between each bin between the two histograms. Ratio values near 1 indicate good agreement for the normalization of the distributions.

The values of $\langle |\epsilon| \rangle$ and δ_ϵ vary for each kinematic distribution, ranging from 0.040 to 0.188, implying that some distributions agree better than others. Distributions such as $M_{\ell\ell}$ and $\not{E}_T$, for example, are ones that have poorer agreement. The values for $\langle |\epsilon| \rangle$ for the sinθ m_{TZZ} distributions are all under 0.1, while the values for δ_ϵ are roughly around 0.1. A 10% systematic uncertainty is therefore retained to account for the shape differences between the DELPHES signal and the ATLAS signal. More about the uncertainties in the fit is discussed in Chapter 6.

The ratio of the total histogram content is used to compare the normalizations. The content ratio for the ee channel distributions is $r = 1.002 \pm 0.011$, while the

content ratio for the $\mu\mu$ channel is $r = 1.015 \pm 0.009$, implying good agreement for the final normalization of the DELPHES distributions with respect to the ATLAS distributions for 139 fb^{-1}.

Distribution	χ^2/NDF	$\langle\|\epsilon\|\rangle$	δ_ϵ	Ratio
m_{TZZ}	66.5/20	0.052	0.083	1.002 ± 0.011
m_{TZZ} (fine)	172.2/92	0.070	0.121	1.002 ± 0.011
M_{ll}	264.8/14	0.161	0.176	1.002 ± 0.011
$\not{E}_T$	291.2/19	0.126	0.174	1.002 ± 0.011
H_T	109.8/45	0.085	0.112	1.002 ± 0.011
pT_{l1}	125.9/45	0.053	0.104	1.002 ± 0.011
pT_{l2}	174.5/32	0.084	0.129	1.002 ± 0.011
pT_{ll}	188.3/42	0.079	0.139	1.002 ± 0.011
ΔR_{ll}	138.6/20	0.063	0.121	1.002 ± 0.011

Table 3.4: χ^2/NDF, $\langle|\epsilon|\rangle$ δ_ϵ, and total content ratio for ee channel distributions for $\sin\theta = 0.7$. The second m_{TZZ} quantity has finer binning, as shown in Figure 3.4.

Distribution	χ^2/NDF	$\langle\|\epsilon\|\rangle$	δ_ϵ	Ratio
m_{TZZ}	65.6/21	0.044	0.073	1.015 ± 0.009
m_{TZZ} (fine)	174.8/93	0.065	0.108	1.015 ± 0.009
M_{ll}	562.1/14	0.188	0.222	1.015 ± 0.009
$\not{E}_T$	275.5/19	0.097	0.148	1.015 ± 0.009
H_T	164.5/45	0.088	0.120	1.015 ± 0.009
pT_{l1}	98.9/44	0.040	0.086	1.015 ± 0.009
pT_{l2}	85.6/32	0.044	0.078	1.015 ± 0.009
pT_{ll}	173.7/43	0.044	0.114	1.015 ± 0.009
ΔR_{ll}	93.1/20	0.037	0.087	1.015 ± 0.009

Table 3.5: χ^2/NDF, $\langle|\epsilon|\rangle$, δ_ϵ, and total content ratio for $\mu\mu$ channel distributions for $\sin\theta = 0.7$. The second m_{TZZ} quantity has finer binning, as shown in Figure 3.4.

$\sin\theta$	χ^2/NDF	$\langle\lvert\epsilon\rvert\rangle$	δ_ϵ	Ratio
0.1	63.1/19	0.092	0.166	0.988 ± 0.023
0.2	53.7/19	0.045	0.080	0.998 ± 0.012
0.3	61.3/19	0.073	0.107	0.991 ± 0.015
0.4	81.4/19	0.066	0.100	1.013 ± 0.011
0.5	70.2/20	0.053	0.085	1.011 ± 0.011
0.6	85.2/19	0.063	0.098	1.011 ± 0.011
0.9	39.4/21	0.060	0.099	1.021 ± 0.018

Table 3.6: χ^2/NDF, $\langle\lvert\epsilon\rvert\rangle$, δ_ϵ, and total content ratio for ee channel m_{TZZ} distributions with non-equidistant binning for various $\sin\theta$ values.

$\sin\theta$	χ^2/NDF	$\langle\lvert\epsilon\rvert\rangle$	δ_ϵ	Ratio
0.1	96.9/21	0.095	0.130	1.027 ± 0.020
0.2	91.8/21	0.059	0.095	0.996 ± 0.010
0.3	80.8/21	0.078	0.108	0.997 ± 0.012
0.4	129.9/22	0.060	0.107	1.008 ± 0.010
0.5	97.7/21	0.054	0.092	1.013 ± 0.010
0.6	160.0/22	0.066	0.115	1.016 ± 0.010
0.9	98.3/21	0.080	0.134	1.012 ± 0.015

Table 3.7: χ^2/NDF, $\langle\lvert\epsilon\rvert\rangle$, δ_ϵ, and total content ratio for $\mu\mu$ channel m_{TZZ} distributions with non-equidistant binning for for various $\sin\theta$ values.

3.3.2 Distributions

Figure 3.3 shows the m_{TZZ} distribution with non-equidistant binning. The binning was chosen to optimize the shape information while minimizing the statistical uncertainty. This binning is also utilized for the m_{TZZ} distributions used as input for the limit setting. The DELPHES and full ATLAS distributions agree well, at the $\delta_\epsilon \sim 10\%$ level; this uncertainty will have a negligible impact on the limit setting. Figure 3.4 shows the same distribution with finer binning.

While only the m_{TZZ} distribution is relevant for limit setting, DELPHES ability to emulate other observables is of interest. Figures 3.5 and 3.6 show the $\not{E}_T$ and H_T distributions, respectively. These observables are particularly difficult to emulate as they are global variables that depend on various factors present throughout the detector. Despite this, the shapes agree at the $\delta_\epsilon \sim 16\%$ level for $\not{E}_T$ and at the $\delta_\epsilon \sim 12\%$ level for H_T.

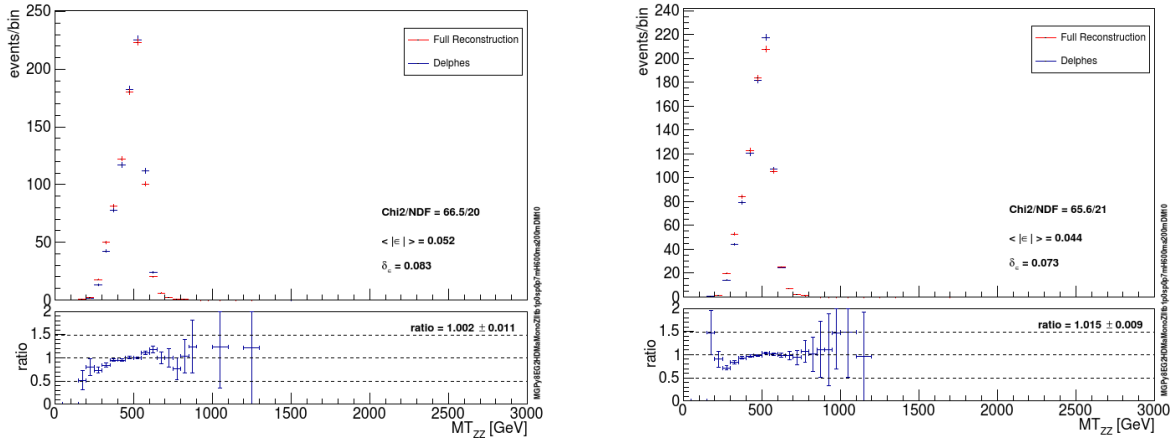

(a) ee signal region.

(b) $\mu\mu$ signal region.

Figure 3.3: m_{TZZ} with non-equidistant binning for ee and $\mu\mu$ channels, respectively, for $\sin\theta = 0.7$. The red distributions are from the fully reconstructed samples, while the blue distributions are the normalized DELPHES distributions.

Figure 3.7 contains the lepton pair invariant mass for both the ee and $\mu\mu$ channels clearly showing a Z peak. This observable has the poorest shape agreement among all of the studied kinematic distributions. The widths are approximately equal, centered about the Z boson mass $m_Z \approx 91$ GeV [1], however the peaks do not agree well. This could be due to DELPHES not correctly simulating the angular resolution of each lepton. These distributions have the largest values for $\langle|\epsilon|\rangle$ and δ_ϵ as seen in Tables 3.4 and 3.5. The shape differences were found to have a negligible impact on the final limit results, as will be shown in Chapter 6.

Overall, DELPHES reproduces rather well the kinematic distributions of the fully reconstructed samples, especially m_{TZZ}. More kinematic distributions can be found in Appendix C.

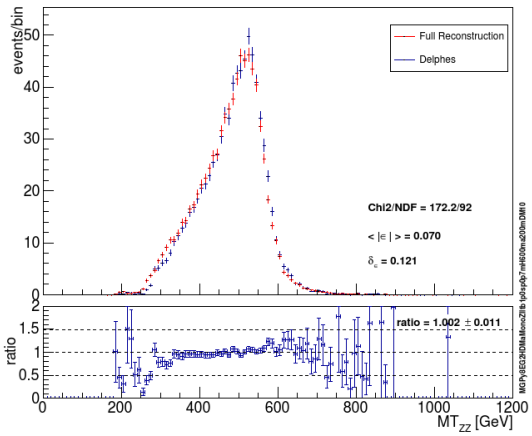

(a) ee signal region.

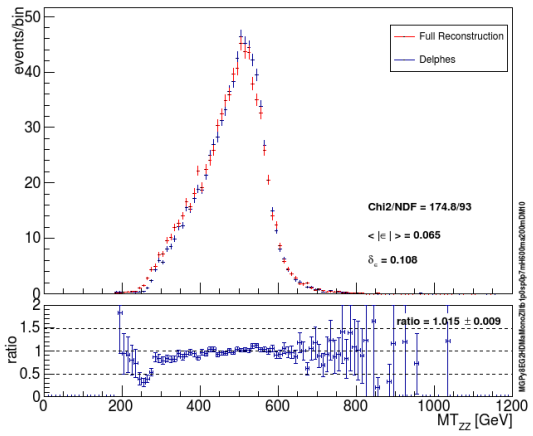

(b) $\mu\mu$ signal region.

Figure 3.4: m_{TZZ} for ee and $\mu\mu$ channels, respectively, for $\sin\theta = 0.7$, using a finer binning for display only.

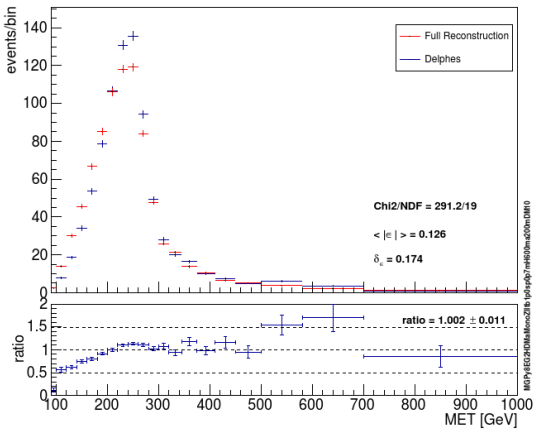

(a) ee signal region.

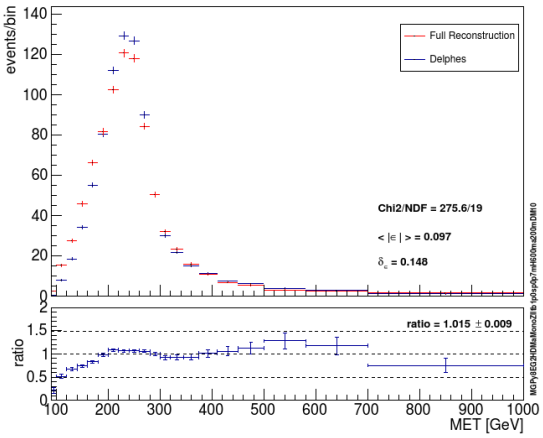

(b) $\mu\mu$ signal region.

Figure 3.5: $\not{E}_T$ for ee and $\mu\mu$ channels, respectively, for $\sin\theta = 0.7$.

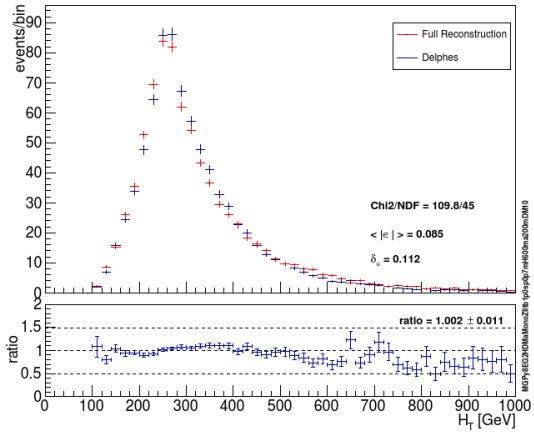

(a) ee signal region.

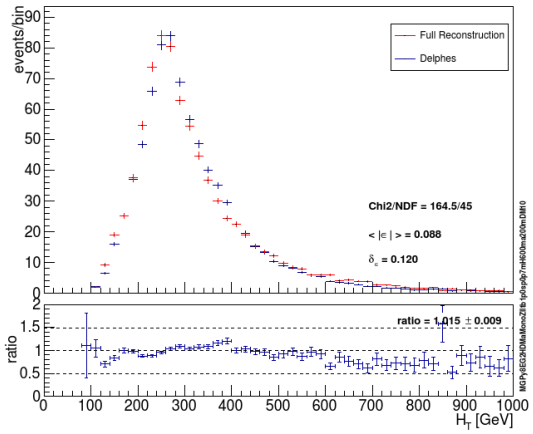

(b) $\mu\mu$ signal region.

Figure 3.6: H_T for ee and $\mu\mu$ channels, respectively, for $\sin\theta = 0.7$.

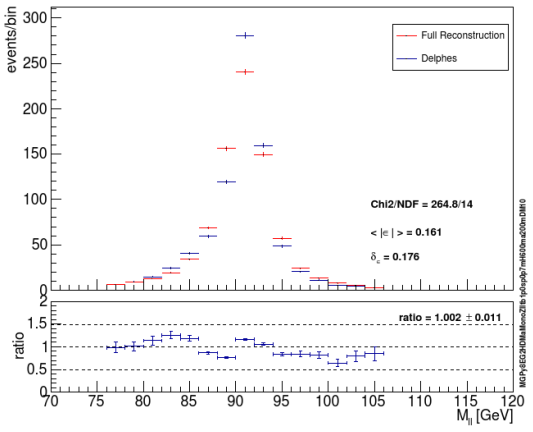

(a) ee signal region.

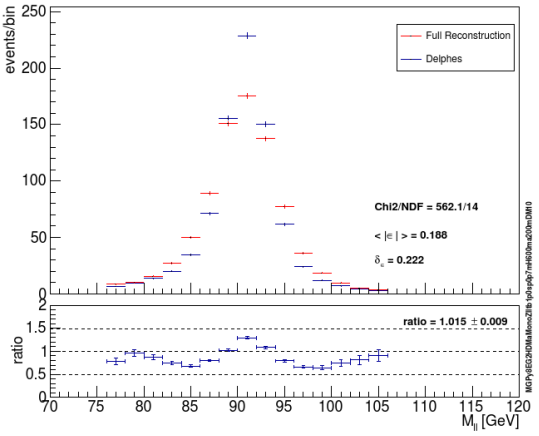

(b) $\mu\mu$ signal region.

Figure 3.7: Z invariant mass for ee and $\mu\mu$ channels, respectively, for $\sin\theta = 0.7$.

Chapter 4

Backgrounds and systematics

Many Standard Model background processes produce the same signature as the two Higgs doublet dark matter model. Therefore, as mentioned in Chapter 2, selection cuts on the data are made in attempt to reduce the backgrounds as much as possible while maximizing the signal. The selection cuts made in this analysis and the backgrounds they reduce are listed in Table 2.1. Systematic uncertainties affect the backgrounds as well as the signal, which are classified into two groups - theoretical and experimental. This chapter describes the different backgrounds to the Mono-Z search and their systematic uncertainties, and follows [41].

Table 4.1 describes the percent contribution from each background to the total background yield as well as how they are estimated. The largest background contribution is from ZZ final states, from the processes $qq \to ZZ \to \ell^+\ell^-\nu\overline{\nu}$, $qq \to ZZ \to \ell^+\ell^-\nu\overline{\nu}jj$, and $gg \to ZZ \to \ell^+\ell^-\nu\overline{\nu}$. Here, both leptons are detected while the neutrinos are a source of $\not{E}_T$. The ZZ background is irreducible, accounts for 59% of the total background and is most reliably estimated by simulation.

Background	Percent contribution	Estimation procedure
ZZ	59%	Simulation
WZ	25%	Simulation and data
Z + jets	8%	Data
Non-resonant	8%	Simulation and data
$ttV(V)$, VVV	<1%	Simulation

Table 4.1: Background types and percent contribution to the total background.

The second largest background is the WZ final state with the process $WZ \to \ell\nu\ell\ell$ which occurs when the lepton from the W boson is not reconstructed. The event is then not filtered out by the third-lepton veto event selection step, and the neutrino

and the missed lepton produce $\not{E}_T$. It accounts for 25% of the total background and is estimated by a combination of simulation and data.

The Z+jets final state makes up 8% of the total background, where the $\not{E}_T$ occurs from jet mismodelling. It is difficult to model accurately, and by consequence, difficult to estimate. Therefore, the best estimates are obtained from data. In this thesis, the Z+jets background is estimated using a γ+jets reweighting technique developed by [41], which has a lower statistical uncertainty than the Z+jets estimate obtained using conventional means.

Another main background is the non-resonant final state. This particular type of background can originate from several processes, such as WW, Wt and $t\bar{t}$ and is estimated by a combination of simulation and data. These processes become a source of background when they produce two same flavour leptons with opposite signs along with neutrinos that produce significant $\not{E}_T$. The smaller backgrounds, such as ttV, $ttVV$ and VVV, make up less than 1% of the total background and are estimated by simulation.

The m_{TZZ} distributions, as seen in Figure 4.1, are used in this dark matter search. Stacked background histograms are shown in different colours, while the red squares on the bottom sections of the plots are the ratios of data over the model background estimates.

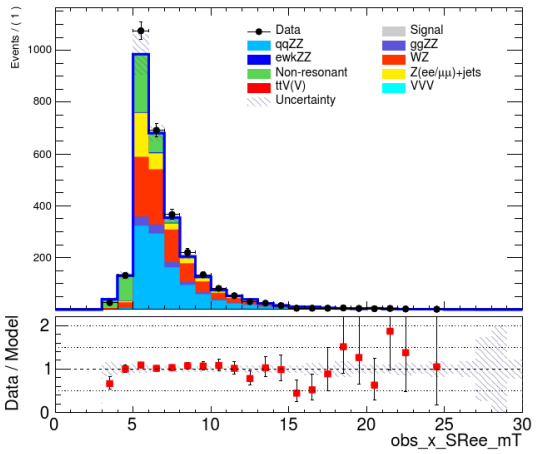

(a) Pre-fit background distribution for ee channel.

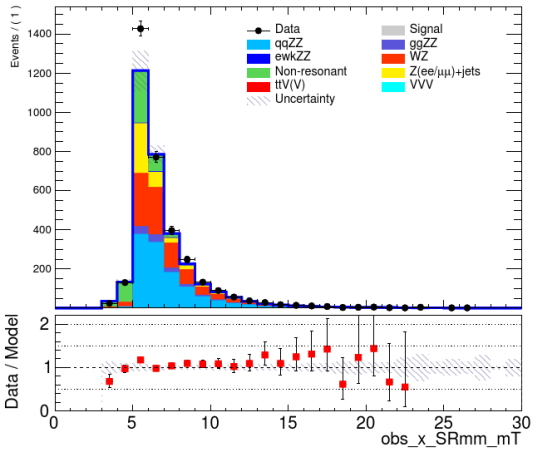

(b) Pre-fit background distribution for $\mu\mu$ channel.

Figure 4.1: m_{TZZ} distributions of a background-only fit for $\sin\theta = 0.7$.

Systematic uncertainties affect our knowledge of the background distributions and are divided into two groups - theoretical and experimental - both of which affect yields

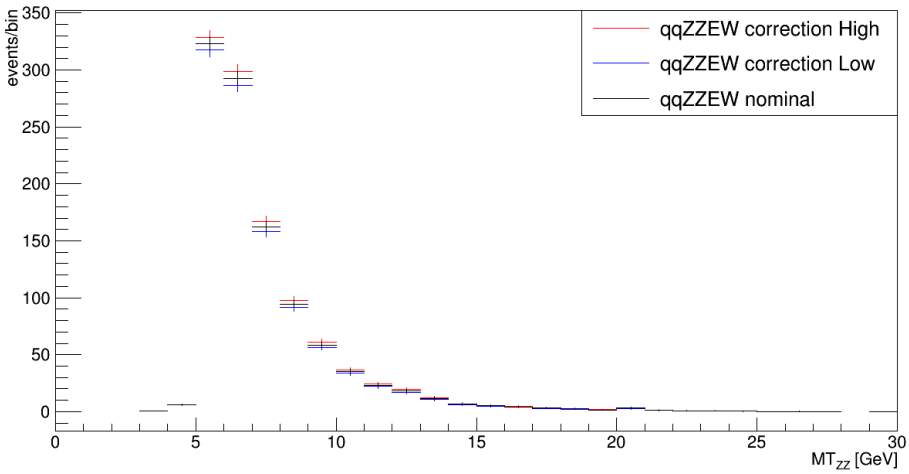

Figure 4.2: m_{TZZ} distribution with electroweak high (red) and low (blue) corrections to the nominal (black) $qqZZ$ background.

and the shape of the discriminant variable distributions. Theoretical systematics, such as QCD scale, parton distribution function (PDF) and parton shower uncertainties are from the variations in cross section calculations, while experimental systematics are related to detector reconstruction uncertainties. Systematic uncertainties are implemented as variations of the nominal distribution of the discriminant variable m_{TZZ}. Each variation is used as input into the fitting procedure and correspond to a nuisance parameter. Figure 4.2 shows an example of a systematic variation of the $qqZZ$ m_{TZZ} background distribution with the high and low systematic variations from theoretical electroweak corrections.

The top ranking theoretical systematics for each background type, as well as the top experimental systematics, are listed in Table 4.2. The PSSignal systematic is the combined uncertainty on the Mono-Z signal for QCD, PDF and parton showering effects. The QCD theoretical systematics, such as qqZZQCDscale, ggZZQCDscale, var_th_QCD, ttbarQCD and QCD arise from variations of the renormalization and factorization scales on the backgrounds. The PDF theoretical systematics, such as EWKZZPDF and var_th_MUR1_MUF1_PDF, are due to uncertainties in the PDF calculation. The photonZjets systematics, such as photonZjetsExpSys, photonZjetsMisModellingSys, photonZjetsStatSys, photonZjetsTheorySys, photonZjetsMCNonClosureSys and photonZjetsSubtractionSys are due to uncertainties in the γ+jets reweighting procedure used to estimate the Z+jets background as described in [41]. The systematics qqZZPSCKKW, qqZZPSCKIN, qqZZPSQSF and ggZZPSQSF are related to parton showering uncertainties. The remaining systematics from Table

Background	Systematic	Type
SignalTh	PSSignal	Theoretical
$qqZZ$	qqZZEWcorr	Theoretical
$qqZZ$	qqZZQCDscale	Theoretical
$qqZZ$	qqZZPSCKKW	Theoretical
$qqZZ$	qqZZPSCKIN	Theoretical
$qqZZ$	qqZZPSQSF	Theoretical
$ggZZ$	ggZZQCDscale	Theoretical
$ggZZ$	ggZZPSQSF	Theoretical
Electroweak ZZ	EWKZZPDF	Theoretical
WZ	var_th_QCD	Theoretical
WZ	var_th_MUR1_MUF1_PDF	Theoretical
Z+jets	photonZjetsExpSys	Theoretical
Z+jets	photonZjetsMisModellingSys	Theoretical
Z+jets	photonZjetsStatSys	Theoretical
Z+jets	photonZjetsTheorySys	Theoretical
Z+jets	photonZJetsMCNonClosureSys	Theoretical
Z+jets	photonZjetsSubtractionSys	Theoretical
Non-resonant	ttbarQCD	Theoretical
ttV	QCD	Theoretical
VVV	QCD	Theoretical
-	EG_SCALE_ALL	Experimental
-	MUON_SAGITTA_RESBIAS	Experimental
-	Jet_Pileup_RhoTopology	Experimental
-	PRW_DATASF	Experimental
-	Jet_Flavor_Composition	Experimental

Table 4.2: Top systematic uncertainties from the full ATLAS analysis for each background type. SignalTh is the uncertainty on the signal.

4.2 are experimental and are related to detector uncertainties.

Chapter 5

Statistical treatment for limit setting

5.1 Frequentist profile likelihood test

There exist various statistical tests that can be used to quantify the level of agreement between an experimental measurement and the expected signal (or background) hypothesis, such as the frequentist profile likelihood test. This test is one of the most frequently used tests in experimental particle physics and is based around the profile likelihood ratio [48]. In order to perform a discovery hypothesis test, the profile likelihood ratio can be used to calculate a discovery statistic q_0, which in turn is used to calculate a discovery p-value p_0. The p-value, along with its equivalent significance Z, are used as the main quantities in assessing the validity of a hypothesis. The profile likelihood ratio can also be used to calculate a test statistic $\tilde{q}_\mu$ in order to set upper limits on the signal strength μ. The following describes how these quantities are computed in the asymptotic limit and follows [49].

5.1.1 Likelihood function and profile likelihood ratio

To build the profile likelihood ratio, one must first define the likelihood function. Consider an expected number of events given by $\nu_j = \mu s_j + b_j$, where μ is the signal strength, s_j is the expected signal yield and b_j is the expected background yield for bin j. Then the likelihood is

$$L(\mu, \boldsymbol{\theta}) \quad = \quad \prod_j^N \frac{(\mu s_j + b_j)^{n_j}}{n_j!} e^{-(\mu s_j + b_j)} \times \prod_k^M G(\theta_{j,k}) \tag{5.1}$$

where n_j is the number of measured events for bin j, and $\theta_{j,k}$ are Gaussian distributed nuisance parameters.

Maximum likelihood estimators (MLE) are the values of the parameters that maximize the likelihood function. We can denote the *unconditional* MLE of the signal strength μ and the nuisance parameters $\boldsymbol{\theta}$ as $\hat{\mu}$ and $\hat{\boldsymbol{\theta}}$. For a given μ, we obtain the *conditional* MLE of $\boldsymbol{\theta}$, which is denoted as $\hat{\hat{\boldsymbol{\theta}}}$.

In order to test the hypothesis for $\hat{\mu}$ against other hypotheses, one uses the profile likelihood ratio which quantifies the agreement between the observed $\hat{\mu}$ and the μ hypothesis in question. The profile likelihood ratio is the ratio between the likelihoods of $\hat{\hat{\boldsymbol{\theta}}}$ with a given μ, and the MLE of μ and $\boldsymbol{\theta}$:

$$\lambda(\mu) = \frac{L(\mu, \hat{\hat{\boldsymbol{\theta}}}(\mu))}{L(\hat{\mu}, \hat{\boldsymbol{\theta}})}. \tag{5.2}$$

The ratio can be between $0 \leq \lambda(\mu) \leq 1$, with values close to 1 implying good agreement between the two hypotheses.

5.1.2 Discovery statistics

In order to test for evidence of a positive signal, a discovery hypothesis test is performed. This is done by first computing the discovery test statistic, q_0:

$$q_0 = \begin{cases} -2\ln\lambda(0) & \hat{\mu} \geq 0 \\ 0 & \hat{\mu} < 0 \end{cases} \tag{5.3}$$

where $\lambda(0)$ is the profile likelihood ratio evaluated for $\mu = 0$. To quantify the level of agreement between the signal+backgound hypothesis and the data, q_0 can be used to obtain the discovery p-value, given by

$$p_0 = \int_{q_{0,\text{obs}}}^{\infty} f(q_0|0) dq_0. \tag{5.4}$$

where $q_{0,\text{obs}}$ is the value of q_0 obtained from the data, and $f(q_0|0)$ is the probability distribution function (PDF) of q_0 for $\mu = 0$. In the asymptotic limit, or in the limit of large N (from Equation 5.1), the PDF can be obtained analytically. A large enough p-value indicates that the data agrees with the null hypothesis, and no discovery can be claimed.

In experimental particle physics, the p-value is often translated into a value called

the significance Z, defined as

$$Z = \Phi^{-1}(1-p) \tag{5.5}$$

where Φ^{-1} is the inverse of the cumulative distribution, or quantile of the standard Gaussian function. The significance of a hypothesis determines if said hypothesis is rejected or not. The standard significance for rejecting a background only hypothesis H_0, and accepting a scientific discovery, is $Z = 5$, which is consistent with a p-value of 2.87×10^{-7}. A significance of $Z = 3$ conveys that there is evidence for a discovery. On the contrary, for setting exclusion limits for a model's parameters, the standard significance for rejecting a signal hypothesis H is $Z = 1.64$. This is consistent with a p-value of $p = 0.05$, and thus a 95% confidence level (CL).

5.1.3 Statistics for limit setting

In the case where no discovery can be claimed from the discovery hypothesis test, one can set an upper limit on the signal strength μ using the CL_s method. To do so, we first define the alternative test statistic $\tilde{q}_\mu$ as

$$\tilde{q}_\mu = \begin{cases} -2\ln\frac{L(\mu,\hat{\hat{\boldsymbol{\theta}}}(\mu))}{L(0,\hat{\hat{\boldsymbol{\theta}}}(0)} & \hat{\mu} < 0 \\ -2\ln\frac{L(\mu,\hat{\hat{\boldsymbol{\theta}}}(\mu))}{L(\hat{\mu},\hat{\boldsymbol{\theta}})} & 0 \leq \hat{\mu} \leq \mu \\ 0 & \hat{\mu} > \mu. \end{cases} \tag{5.6}$$

The p-value, which is the probability to observe a $\tilde{q}_\mu$ greater than or equal to $\tilde{q}_{\mu,\mathrm{obs}}$, can then be obtained:

$$p_\mu = \int_{\tilde{q}_{\mu,\mathrm{obs}}}^{\infty} f(\tilde{q}_\mu|\mu)d\tilde{q}_\mu. \tag{5.7}$$

The p-value for the CL_s method, or the CL_s value, is then defined as

$$\mathrm{CL}_s = \frac{\mathrm{CL}_{s+b}}{\mathrm{CL}_b} = \frac{p_{s+b}}{1-p_b} \tag{5.8}$$

where

$$p_{s+b} = \int_{\tilde{q}_{\mu,\mathrm{obs}}}^{\infty} f(\tilde{q}_\mu|\mu=1)d\tilde{q}_\mu \tag{5.9}$$

is the p-value for the signal+background hypothesis, and

$$p_b = \int_{\tilde{q}_{\mu,\mathrm{obs}}}^{\infty} f(\tilde{q}_\mu|\mu = 0)d\tilde{q}_\mu \tag{5.10}$$

is the p-value for the background-only hypothesis.

5.1.4 Upper limit on the signal strength μ_{up}

The upper limit on the signal strength for a given parameter point, μ_{up}, is the value of μ that gives a CL_s value of $\mathrm{CL}_s = 0.05$. This corresponds to a 95% confidence level. Therefore, μ values that correspond to $\mathrm{CL}_s < 0.05$ can be excluded at a 95% CL, as smaller CL_s values correspond to the data agreeing with the background-only hypothesis. Figure 5.2 shows how the CL_s, CL_{s+b} and CL_b values change with μ. The expected $\mu_{\mathrm{up}}^{95\%}$, the upper limit on μ at a 95% CL, is obtained by finding where the expected CL_s is for a p-value of $p = 0.05$. The observed $\mu_{\mathrm{up}}^{95\%}$ is then obtained by the observed CL_s value for a p-value of $p = 0.05$.

For large N, the value for μ_{up} can be approximated by

$$\mu_{\mathrm{up}} = \hat{\mu} + \sigma\Phi^{-1}(1 - \alpha) \tag{5.11}$$

where, for a p-value below a certain threshold α, μ is excluded at CL of $1 - \alpha$. Here, σ is obtained from the Wald approximation, which states that [50]

$$-2\ln\lambda(\mu) = \frac{(\mu - \hat{\mu})^2}{\sigma^2} + \mathcal{O}\left(\frac{1}{\sqrt{N}}\right) \tag{5.12}$$

where $\hat{\mu}$ is Gaussian-distributed with a standard deviation σ and mean μ', for a μ' that can be different than the hypothesized μ. HistFitter computes the μ_{up} values for the parameter points of interest and uses those to create limit plots. More on HistFitter can be found in the next section.

5.2 Statistical treatment software

HistFitter is a software used for data analysis that can be used to compute the statistical quantities defined in Section 5.1, in which the user configures an input file composed of various signal and backgound histograms [51]. HistFitter takes the model information and creates a workspace for the given model, and takes into con-

sideration the sample, channel, region (control, signal or validation) and systematic uncertainties. The information is passed on to a software package called HistFactory, which builds a probability density function (PDF) for the combined histograms. The PDFs are then passed to other ROOT packages called RooFit and RooStats to conduct statistical analysis on the data. An overview of the HistFitter processing scheme can be found in Figure 5.1.

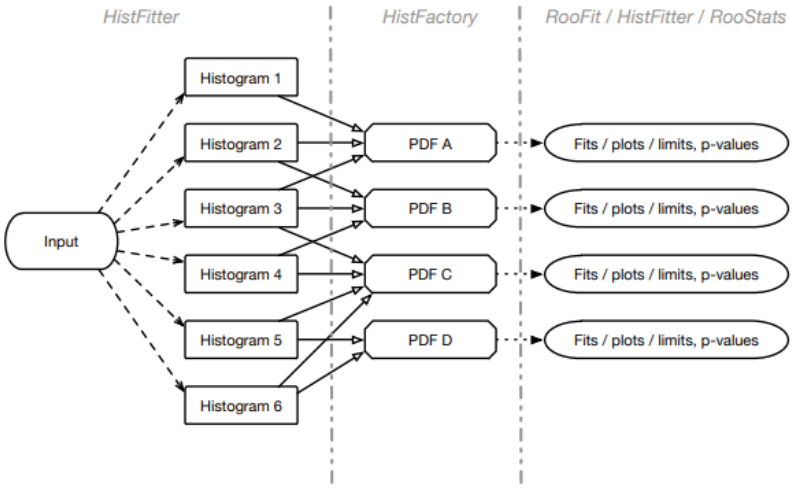

Figure 5.1: Overview of HistFitter treatment of inputs [51].

HistFitter is able to compute the p-value for a given signal model ($\mu = 1$) along with the corresponding CL_b, CL_s and CL_{s+b} values, and is also able to compute the null p-value and significance. It can also compute the expected μ_{up} along with the median, $\pm 1\sigma$ and $\pm 2\sigma$ bands. An asymptotic CL scan for $\sin\theta = 0.4$ can be found in Figure 5.2, which shows the observed CL_s, CL_{s+b}, CL_b and expected median CL_s as a function of the signal parameter μ. All of these quantities can be used as input to create limit plots, which are discussed in Chapter 6.

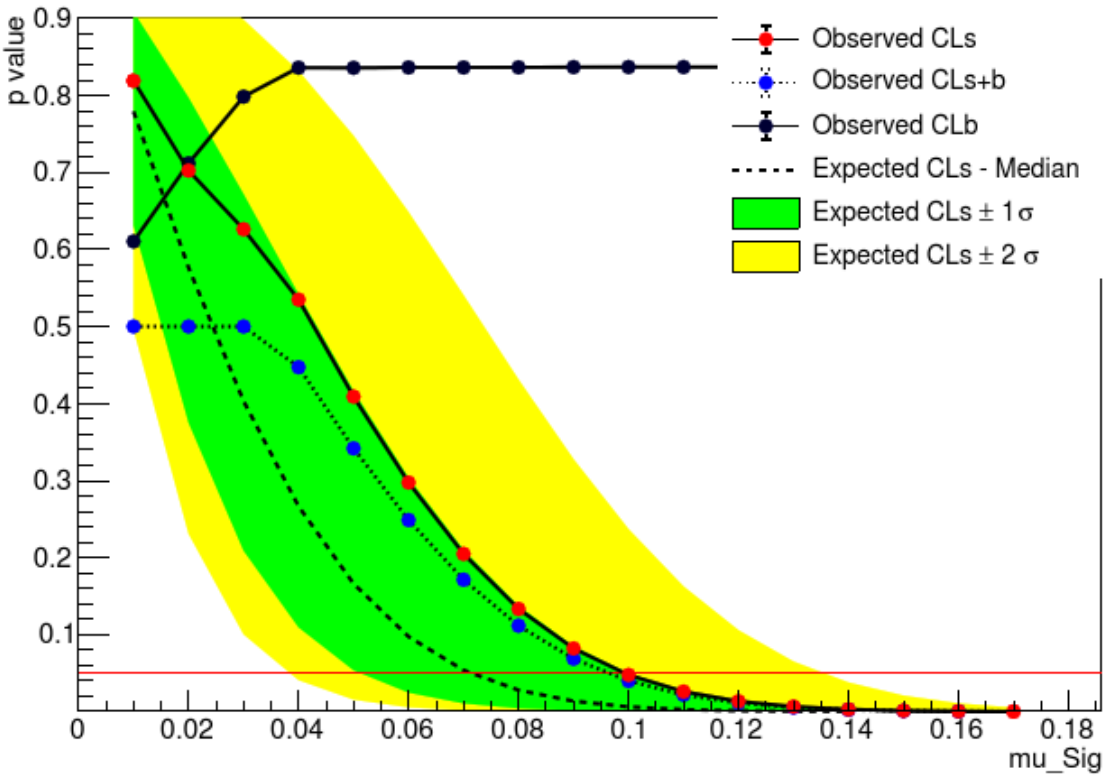

Figure 5.2: Asymptotic CL scan for $\sin\theta = 0.4$.

Chapter 6

Results

This chapter introduces sinθ signal strength limits obtained by using the DELPHES signal for different sets of systematics. First, the DELPHES signal is used with the full list of systematics and compared to the limits produced by the full ATLAS simulation. Then, two different cases of reduced systematics are considered; the yields, ranking plots, pull plots and sinθ limit scans for both cases are used to assess the effect of reducing the systematics.

6.1 Limit comparison

As described in Chapter 5, HISTFITTER takes signal and background histograms as input in order to compute signal strength limits. To compare the DELPHES analysis method to the full ATLAS analysis, DELPHES signal distributions are used as input for a 2HDMa sinθ parameter scan with the complete list of just over 100 systematics used in the full analysis. Table 6.1 contains the pre- and post-fit yields for the limit using the DELPHES signal for sin$\theta = 0.7$, where the signal+background are fitted to the data separately for both signal regions (SR) ee and $\mu\mu$. The errors given are the statistical and systematic errors added in quadrature. The yields for the ATLAS scan can be found in Table 6.2 for comparison. The background yields after the fit are virtually identical as expected. The signal yields are 28 ± 26 for the ee SR and 28 ± 27 for the $\mu\mu$ SR for the DELPHES signal sample. The signal yields after the fit for the ATLAS signal sample are 24 ± 22 for the ee SR and 24 ± 23 for the $\mu\mu$ SR. Both results agree with the background only hypothesis.

The limit scan using the DELPHES signal is shown in Figure 6.1 for tan$\beta = 1.0$, $m_H = 600$ GeV, $m_a = 200$ GeV, and $m_\chi = 10$ GeV at a center-of-mass energy of $\sqrt{s} = 13$ TeV for ee and $\mu\mu$ combined channels. The fully reconstructed ATLAS limit

Table 6.1: Pre- and post-fit yields for $\sin\theta = 0.7$ using a DELPHES signal sample.

	e^+e^-	$\mu^+\mu^-$
Observed events	2881	3409
Yields after fit	2927.03 ± 44.22	3353.73 ± 47.64
$qqZZ$	1058.90 ± 56.57	1211.09 ± 54.62
$ggZZ$	129.20 ± 38.25	143.45 ± 42.36
EWKZZ	18.53 ± 1.28	19.36 ± 1.33
WZ	787.18 ± 26.18	877.87 ± 29.01
Non-res $\ell\ell$	419.51 ± 26.32	475.39 ± 27.20
Z+jets	474.06 ± 64.84	586.19 ± 67.09
$ttV(V)$	6.25 ± 0.79	5.71 ± 0.69
VVV	5.86 ± 0.69	6.23 ± 0.73
Signal	27.54 ± 25.63	28.43 ± 26.65
Yields before fit	3576.73 ± 215.66	3953.71 ± 238.02
$qqZZ$	1056.14 ± 75.73	1199.69 ± 72.58
$ggZZ$	124.99 ± 41.19	138.64 ± 45.50
EWKZZ	18.35 ± 1.31	18.92 ± 1.37
WZ	785.23 ± 32.99	868.87 ± 37.93
Non-res $\ell\ell$	444.50 ± 45.93	499.61 ± 47.11
Z+jets	324.74 ± 132.12	409.26 ± 161.68
$ttV(V)$	6.07 ± 0.82	5.55 ± 0.71
VVV	5.86 ± 0.70	6.20 ± 0.74
Signal	810.85 ± 115.62	806.97 ± 115.06

is shown in Figure 6.2 for the same fixed parameters for comparison purposes. The $\sin\theta$ values are located on the horizontal axis while the vertical axis is the upper limit on μ at a 95% CL. The blue dashed line is the expected limit obtained from Run I which consists of 36 fb^{-1} of data. The black dashed line is the expected limit, while the solid black line is the measured limit from Run II data with 139^{-1} fb. The green and yellow solid bands are the $\pm1\sigma$ and $\pm2\sigma$ bands, respectively. All parameter points located above the black dashed line can be excluded. The limits obtained using the ATLAS full simulation and obtained using DELPHES are approximately equal. This can be seen in Table 6.5, which displays the numerical expected limits for each parameter point for both cases.

Table 6.2: Pre- and post-fit yields for the ATLAS fit for $\sin\theta = 0.7$. The pre-fit background yields are the same as in Table 6.1.

	e^+e^-	$\mu^+\mu^-$
Observed events	2881	3409
Yields after fit	2927.65 ± 42.69	3353.48 ± 45.74
$qqZZ$	1058.43 ± 57.03	1210.00 ± 55.23
$ggZZ$	129.87 ± 38.34	144.20 ± 42.45
EWKZZ	18.53 ± 1.27	19.34 ± 1.32
WZ	789.93 ± 25.36	880.75 ± 28.26
Non-res $\ell\ell$	419.37 ± 26.27	475.24 ± 27.14
Z+jets	475.28 ± 64.24	587.65 ± 66.43
$ttV(V)$	6.23 ± 0.78	5.70 ± 0.68
VVV	5.87 ± 0.69	6.23 ± 0.72
Signal	24.15 ± 22.30	24.37 ± 22.51
Yields before fit	3577.99 ± 215.73	3965.62 ± 238.90
Signal	812.11 ± 115.78	818.88 ± 116.75

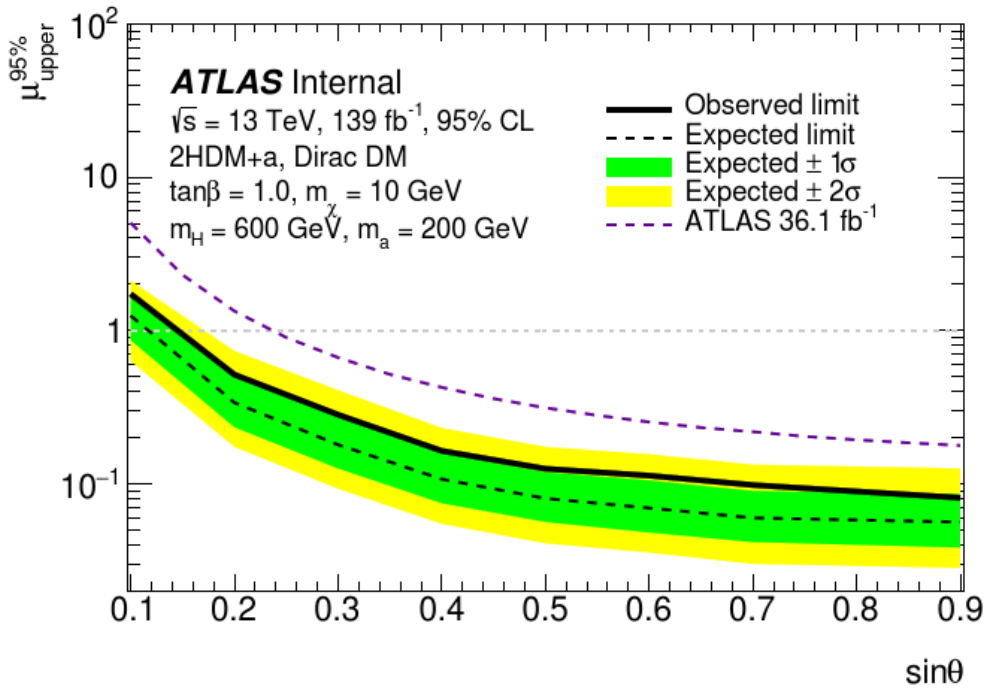

Figure 6.1: sinθ exclusion plot with ee and $\mu\mu$ combined channels using DELPHES signal with full list of systematics.

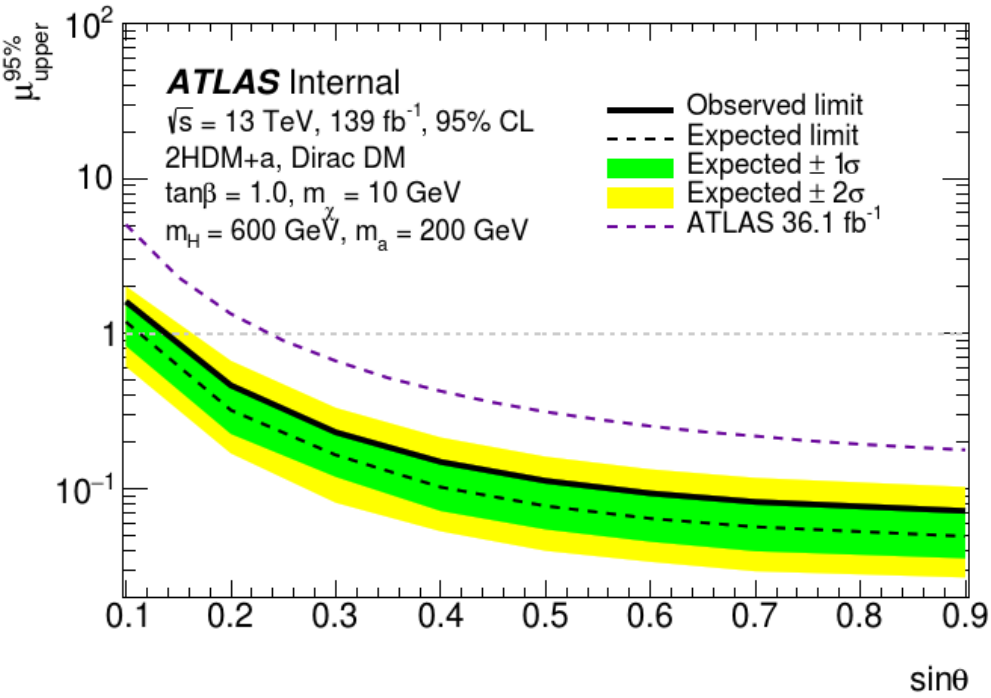

Figure 6.2: sinθ exclusion plot with ee and $\mu\mu$ combined channels using full ATLAS simulation.

6.2 Reduced systematics

Once the DELPHES signal has been used with the full list of systematics, two different cases of reduced systematics are considered. The systematics chosen for these cases are a subset of the systematics from Table 4.2, and each case is listed in Table 6.3. Both cases include at least one systematic for each background type. Following the result of the full ATLAS analysis, a 10% systematic on the signal is assumed from theoretical uncertainties on the acceptance. The differences between DELPHES and ATLAS distributions are included as an overall 10% systematic shape uncertainty, which is a representative estimate of the δ_ϵ values as obtained for the m_{TZZ} distributions in Chapter 3.

		Background	Systematic
1	2		
x	x	SignalTh	10%
x	x	DelphesTh	10% Asymmetric
x	x	$qqZZ$	qqZZEWcorr
x		$qqZZ$	qqZZQCDscale
x		$qqZZ$	qqZZPSCKKW
x		$qqZZ$	lumi
x	x	$ggZZ$	ggZZQCDscale
x		$ggZZ$	lumi
x	x	Electroweak ZZ	EWKZZPDF
x		Electroweak ZZ	lumi
x	x	WZ	var_th_QCD
x		WZ	var_th_MUR1_MUF1_PDF
x		WZ	lumi
x	x	Z+jets	photonZjetsExpSys
x		Z+jets	photonZjetsMisModellingSys
x		Z+jets	photonZjetsStatSys
x		Z+jets	photonZjetsTheorySys
x		Z+jets	lumi
x	x	Non-resonant	ttbarQCD
x		Non-resonant	lumi
x	x	ttV	QCD
x		ttV	lumi
x	x	VVV	QCD
x		VVV	lumi

Table 6.3: HISTFITTER systematics used as inputs for cases 1 and 2. SignalTh is the uncertainty on the signal, while DelphesTh is the shape uncertainty that comes from the differences between the DELPHES and ATLAS kinematic distributions.

Table 6.4: Pre- and post-fit yields for systematics case 1 for $\sin\theta = 0.7$.

	e^+e^-	$\mu^+\mu^-$
Observed events	2881	3409
Yields after fit	2932.43 ± 38.41	3345.10 ± 39.36
$qqZZ$	1037.95 ± 53.65	1183.75 ± 50.04
$ggZZ$	130.63 ± 38.76	144.87 ± 42.81
EWKZZ	18.42 ± 0.53	19.00 ± 0.51
WZ	785.17 ± 1.16	872.54 ± 8.90
Non-res $\ell\ell$	415.28 ± 25.62	469.84 ± 26.35
Z+jets	513.85 ± 55.15	624.25 ± 56.21
$ttV(V)$	6.08 ± 0.67	5.55 ± 0.56
VVV	5.87 ± 0.66	6.21 ± 0.70
Signal	19.18 ± 20.89	19.09 ± 20.79
Yields before fit	3576.73 ± 180.71	3953.71 ± 203.60
$qqZZ$	1056.14 ± 67.83	1199.69 ± 62.49
$ggZZ$	124.99 ± 40.90	138.64 ± 45.19
EWKZZ	18.35 ± 0.54	18.92 ± 0.52
WZ	785.23 ± 1.26	868.87 ± 11.20
Non-res $\ell\ell$	444.50 ± 41.93	499.61 ± 42.72
Z+jets	324.74 ± 131.46	409.26 ± 161.43
$ttV(V)$	6.07 ± 0.67	5.55 ± 0.56
VVV	5.86 ± 0.67	6.20 ± 0.71
Signal	810.85 ± 81.36	806.97 ± 80.86

6.2.1 Systematics case 1

The first result, case 1, is obtained by using the subset of systematics consisting of the top ranking 14 systematics from the full ATLAS reconstruction along with the uncertainty in the luminosity. Table 6.4 contains the pre- and post-fit yields for case 1 for $\sin\theta = 0.7$. While the pre-fit background yields remain the same as in Table 6.1, the error in the pre-fit yields are altered by the change in the systematics list. The signal yield after the fit for systematics case 1 is comparable to the DELPHES result with the full list of systematics, with a yield of 19 ± 21 for the ee and $\mu\mu$ SRs.

The pre- and post-fit m_{TZZ} distributions can be found in Figure 6.3 and 6.4 for ee and $\mu\mu$ channels, respectively. In these figures, the different background types are

stacked, shown in different colours. The signal is shown in grey, while the data is shown as black points. As there is no excess signal observed in the data, the post-fit distributions agree with the background-only hypothesis.

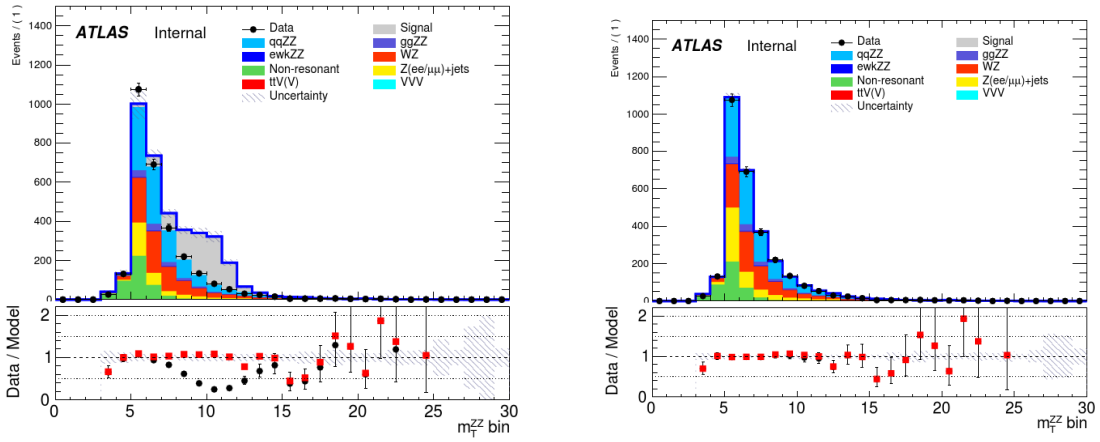

(a) Pre-fit m_{TZZ} distribution. (b) Post-fit m_{TZZ} distribution.

Figure 6.3: Pre- and post-fit m_{TZZ} distribution for ee channel for systematics case 1 with $\sin\theta = 0.7$.

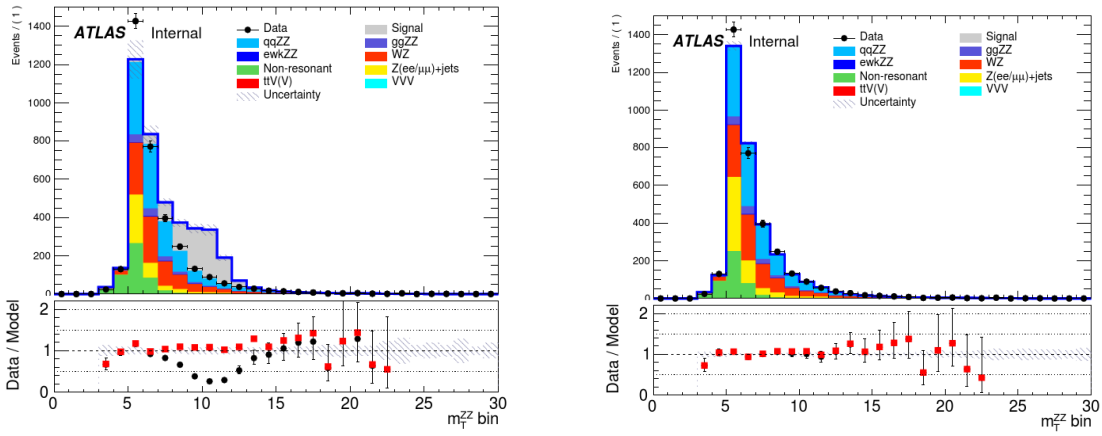

(a) Pre-fit m_{TZZ} distribution. (b) Post-fit m_{TZZ} distribution.

Figure 6.4: Pre- and post-fit m_{TZZ} distribution for $\mu\mu$ channel for systematics case 1 with $\sin\theta = 0.7$.

Figure 6.5 consists of the ranking plot for the nuisance parameters, which shows how much each systematic affects the signal strength μ. The white bar shows the pre-fit impact, $\Delta\mu$, while the grey bar shows the post-fit impact. The top ranking nuisance parameter is one of the Z+jets systematics followed by some of the ZZ and

non-resonant systematics.

The pull plot shown in Figure 6.6 shows how much each systematic was pulled after the fit. The black dot represents the value, while the blue bar represents the error after the fit. As seen in Table 6.4, the Z+jets background has the largest error out of all of the backgrounds, meaning it is allowed to be pulled more than others to better fit the data.

The sinθ scan for systematics case 1 is shown in 6.7, again for ee and $\mu\mu$ combined channels. The observed and expected limits are slightly lower than those obtained using the full list of systematics, meaning more points in the parameter space can be excluded. This result is expected, as there are less uncertainties to account for in the fit. The expected μ_{up} values for the first systematics case can be found in Table 6.5 and can be compared to the ATLAS values found in the same table.

sinθ value	$\mu_{\text{up}}^{\text{exp}}$ (A)	$\mu_{\text{up}}^{\text{exp}}$ (D-Full)	$\mu_{\text{up}}^{\text{exp}}$ (D-1)	$\mu_{\text{up}}^{\text{exp}}$ (D-2)
0.1	1.150	1.247	1.072	1.037
0.2	0.3099	0.3377	0.2875	0.2794
0.3	0.1596	0.1793	0.1462	0.1390
0.4	0.0991	0.1069	0.0941	0.0904
0.5	0.0747	0.0800	0.0711	0.0687
0.6	0.0617	0.0693	0.0583	0.0564
0.7	0.0548	0.0597	0.0517	0.0494
0.9	0.0480	0.0561	0.0451	0.0429

Table 6.5: $\mu_{\text{up}}^{\text{exp}}$ values for tanβ = 0.1, m_H = 600 GeV, m_a = 200 GeV and m_χ = 10 GeV for full ATLAS simulation (A), DELPHES results with the full list of systematics (D-full) and DELPHES systematics cases 1 (D-1) and 2 (D-2).

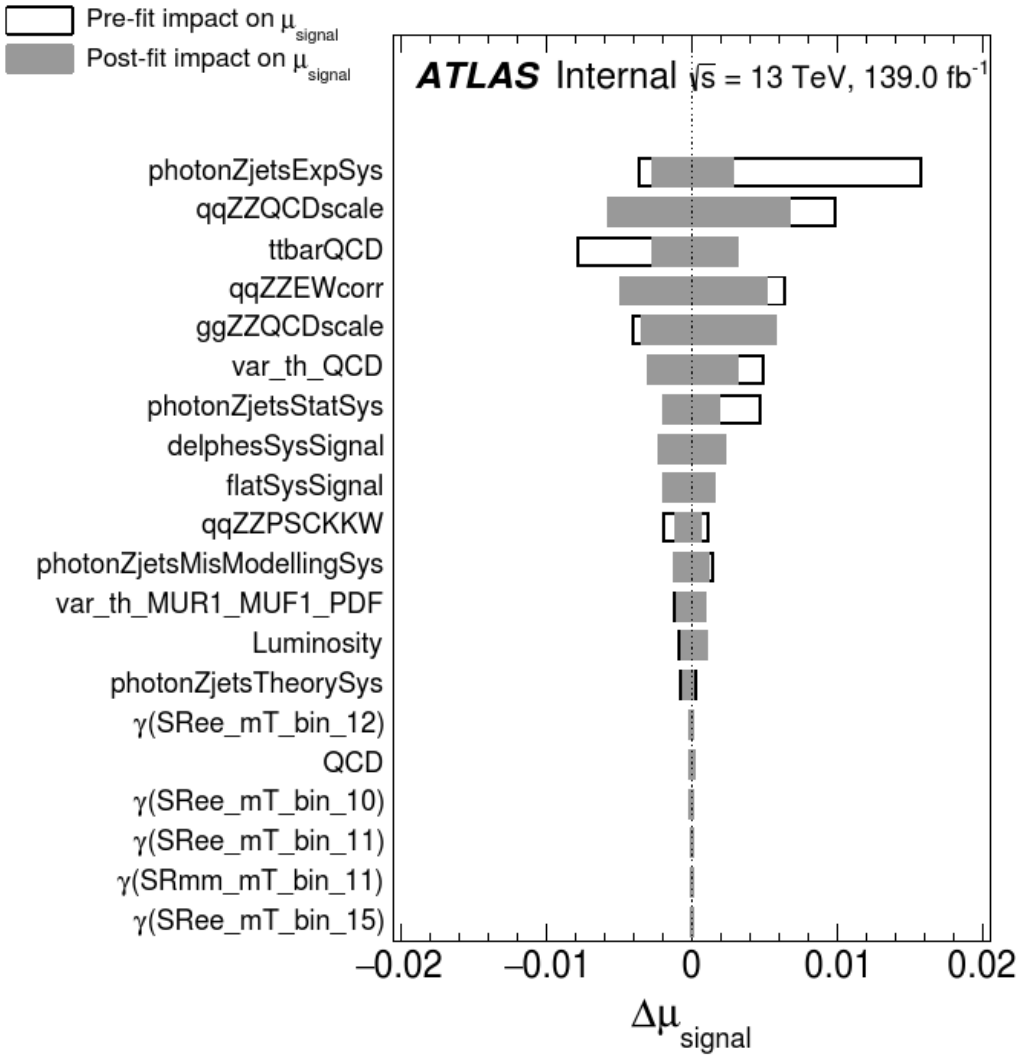

Figure 6.5: Nuisance parameter ranking plot for systematics case 1 with $\sin\theta = 0.7$. The ranking plot takes the numbered m_{TZZ} bins as nuisance parameters and includes them in the plot to show the top 20 ranked parameters.

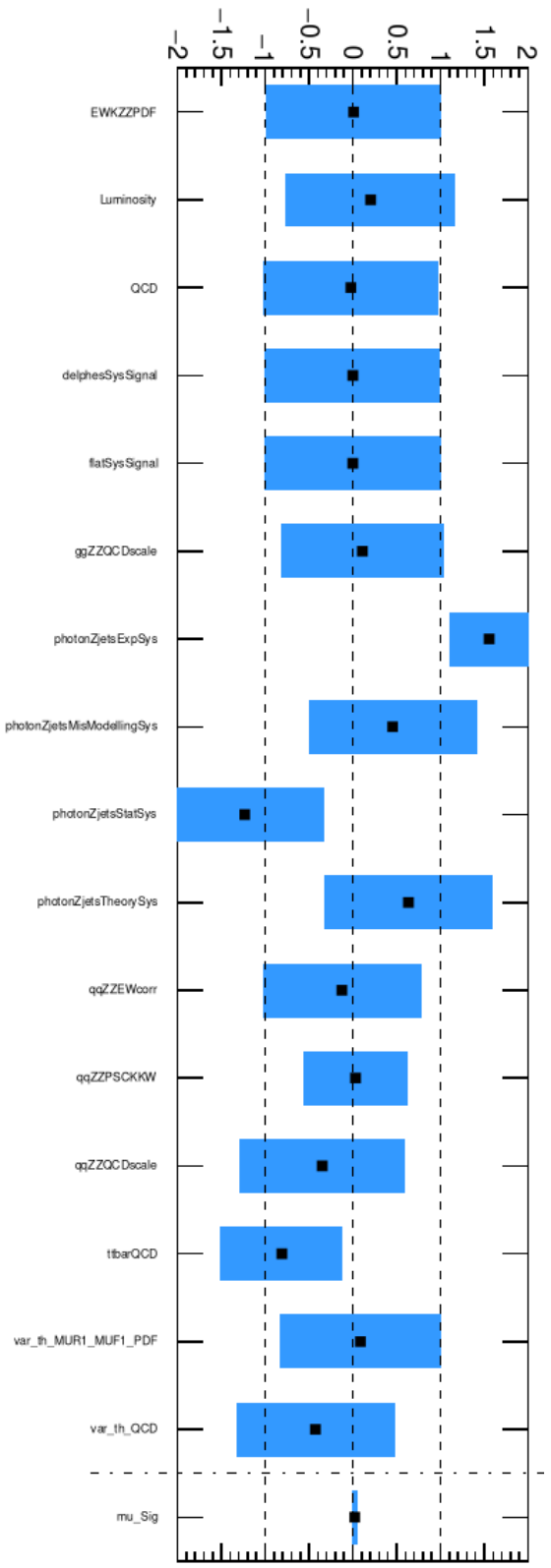

Figure 6.6: Nuisance parameter pull plot for systematics case 1 with $\sin\theta = 0.7$. The Z+jets systematics are pulled more than others due to the background's high error.

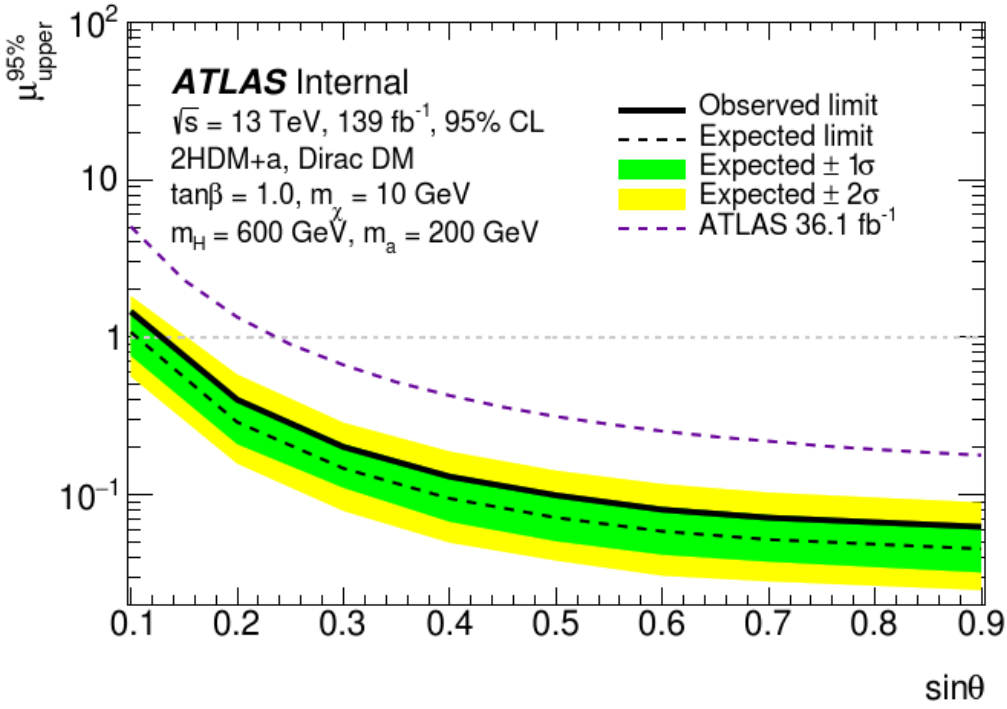

Figure 6.7: $\sin\theta$ exclusion plot with ee and $\mu\mu$ combined channels using DELPHES signal for systematics case 1.

Table 6.6: Pre- and post-fit yields for systematics case 2 for $\sin\theta = 0.7$.

	e^+e^-	$\mu^+\mu^-$
Observed events	2881	3409
Yields after fit	2944.80 ± 36.36	3342.15 ± 39.12
$qqZZ$	1048.81 ± 24.93	1191.63 ± 27.44
$ggZZ$	122.33 ± 34.52	135.70 ± 38.15
EWKZZ	18.35 ± 0.44	18.93 ± 0.41
WZ	785.01 ± 0.22	872.34 ± 7.22
Non-res $\ell\ell$	412.47 ± 24.46	466.80 ± 25.08
Z+jets	531.33 ± 47.02	630.51 ± 50.35
$ttV(V)$	6.06 ± 0.66	5.53 ± 0.55
VVV	5.85 ± 0.65	6.19 ± 0.69
Signal	14.59 ± 19.82	14.52 ± 19.73
Yields before fit	3576.73 ± 157.36	3953.71 ± 185.97
$qqZZ$	1056.14 ± 29.10	1199.69 ± 32.02
$ggZZ$	124.99 ± 40.84	138.64 ± 45.13
EWKZZ	18.35 ± 0.44	18.92 ± 0.41
WZ	785.23 ± 0.52	868.87 ± 9.66
Non-res $\ell\ell$	444.50 ± 41.24	499.61 ± 41.87
Z+jets	324.74 ± 118.00	409.26 ± 152.11
$ttV(V)$	6.07 ± 0.66	5.55 ± 0.55
VVV	5.86 ± 0.66	6.20 ± 0.70
Signal	810.85 ± 81.36	806.97 ± 80.86

6.2.2 Systematics case 2

The systematics case 2 result is obtained by reducing the list of systematics further. It consists of only the main systematic from each background type along with the signal uncertainty and DELPHES uncertainty. The yields for this case can be found in Table 6.6, with the signal yields being 15 ± 20 for the ee and $\mu\mu$ SRs.

The pull plot and ranking plot for case 2 can be found in Figures 6.8 and 6.9, respectively. Similarily to the systematics case 1, the Z+jets background has the largest uncertainty and is pulled the furthest to fit the data. The pre- and post-fit m_{TZZ} distributions can be found in Appendix D, where again, the signal is fit to the background-only hypothesis. The $\sin\theta$ limit scan for systematics case 2 is given in

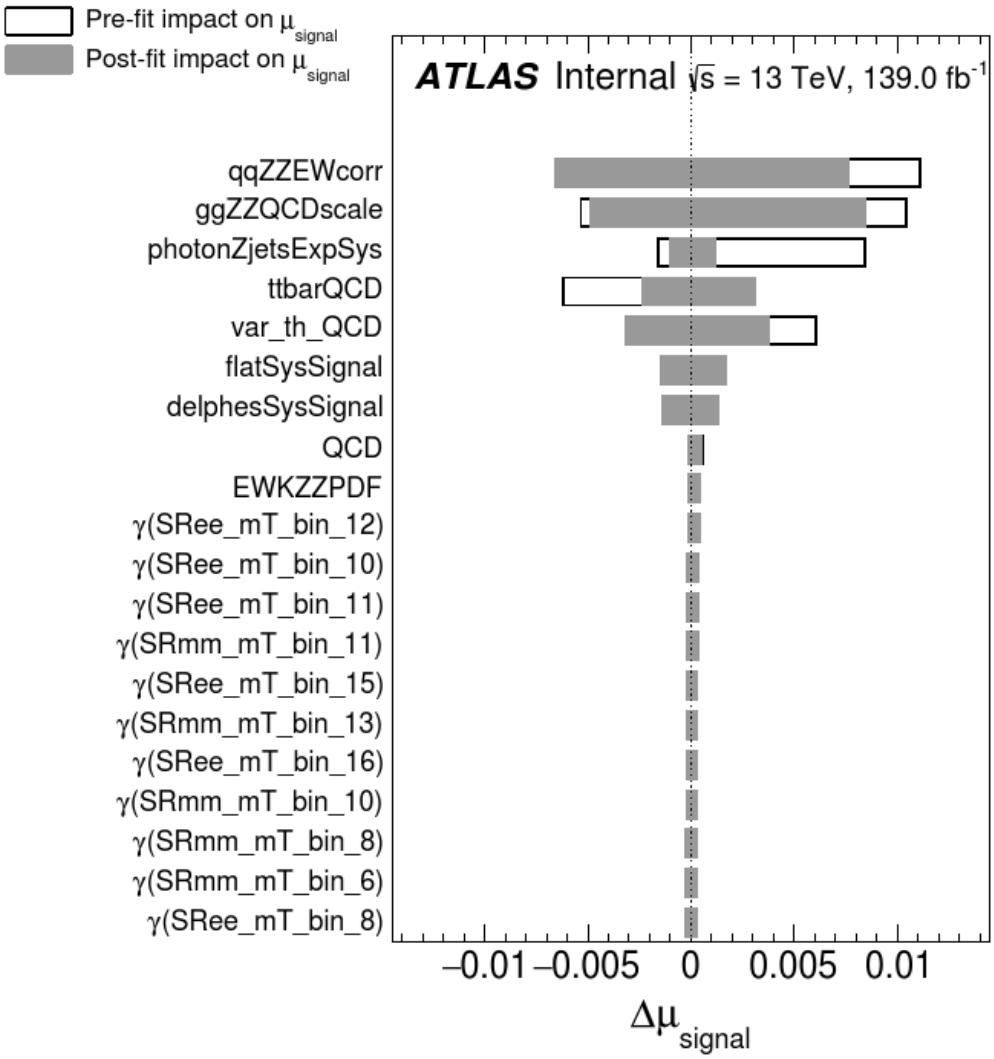

Figure 6.8: Nuisance parameter ranking plot for systematics case 2 with $\sin\theta = 0.7$.

Figure 6.10. The effect on the expected limit is very small in comparison to case 1, however the observed limit does shift lower to a slightly better limit because of the reduced systematics. The expected limits can again be found in Table 6.5. Overall, reducing the list of systematics has a minor effect on both the expected and observed limits for both cases 1 and 2.

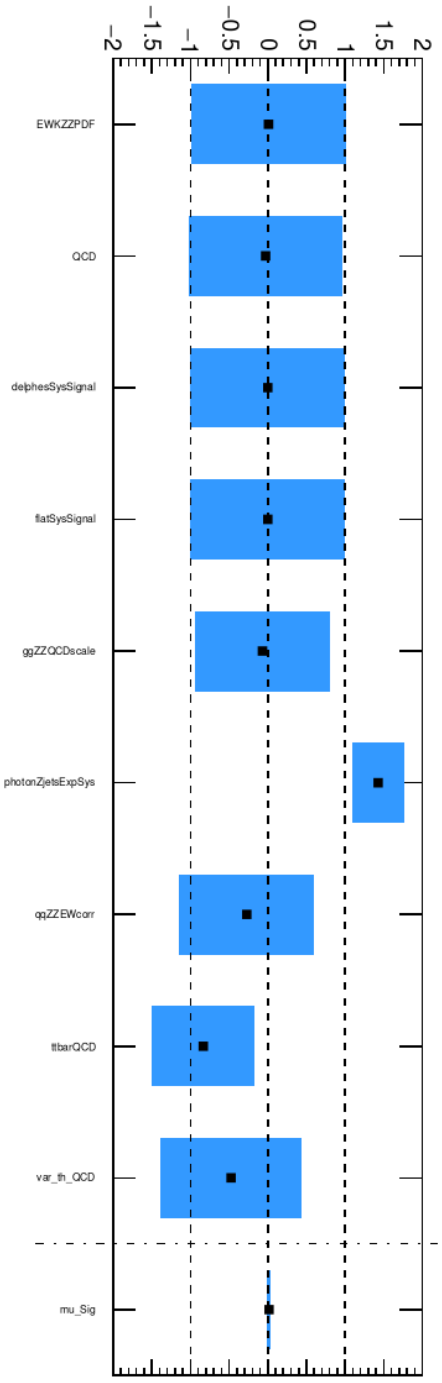

Figure 6.9: Nuisance parameter pull plot for systematics case 2 with $\sin\theta = 0.7$.

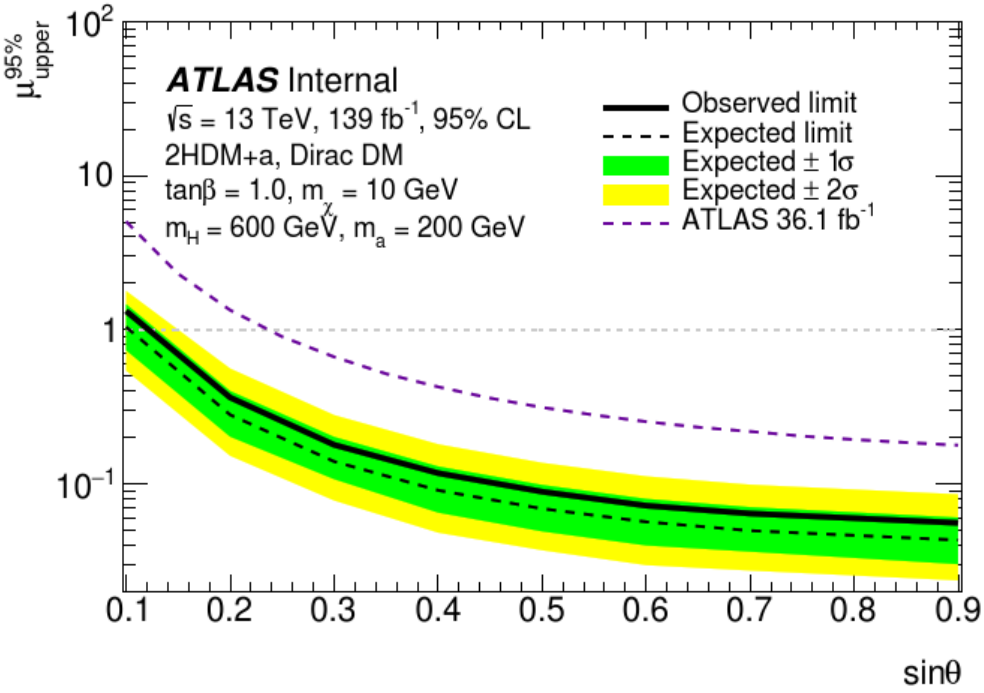

Figure 6.10: sinθ exclusion plot with ee and $\mu\mu$ combined channels using DELPHES signal for systematics case 2.

Chapter 7

Conclusion

There is conclusive astronomical evidence for the existence of gravitationally interacting dark matter in the Universe. However, so far, the existence of a DM particle has not been verified by direct detection, indirect detection or production. Data collected by the ATLAS detector at the LHC are used to search for DM particles. No evidence has been found so far, and limits are obtained on parameters of the two Higgs doublet model with a pseudoscalar.

Signal samples were produced using MadGraph and Pythia, and the ATLAS detector response was simulated using the Delphes software with few changes to the default parameter card. Event selection cuts were applied as in the full ATLAS analysis, and m_{TZZ} is used as the discriminant for the fits. The ee signal region acceptance was found to be too low, leading to an overall scaling factor of 1.7 to be applied to the normalization to account for the low ee count. The shape of the Delphes m_{TZZ} distributions were in good agreement with those obtained using the full ATLAS reconstruction, at the $\sim$ 10% level in bin-by-bin relative differences. Background m_{TZZ} distributions were obtained from the full analysis with focus on the most dominant backgrounds along with their main systematic uncertainties. A frequentist profile likelihood test was used for the statistical treatment of the data. As the discovery hypothesis showed no excess in the full analysis, upper limits were set on the signal strength μ_{up} for the dark matter models of interest. The $\sin\theta$ limit scan produced by the full analysis was closely reproduced with the Delphes signal and less than 20 systematics, reduced from over 100 from the full analysis. The reproduced limit scan was shown to be in good agreement with that obtained by the full analysis.

Future works leading to improvements in the electron acceptance in Delphes as well as in the $M_{\ell\ell}$ shape differences should aim at a better understanding of the

differences between DELPHES and the full ATLAS simulation. The DELPHES fast simulation software and reduced systematics could help in quickly assessing limits in alternative DM model parameters.

Appendix A

Delphes parameter card

The following changes were made to the default DELPHES ATLAS parameter card:

```
######################
# Order of execution of various modules
######################
# Order of execution changed: MissingET moved under UniqueObjectFinder

set ExecutionPath {

  PileUpMerger
  ParticlePropagator

  ChargedHadronTrackingEfficiency
  ElectronTrackingEfficiency
  MuonTrackingEfficiency

  ChargedHadronMomentumSmearing
  ElectronMomentumSmearing
  MuonMomentumSmearing

  TrackMerger
  Calorimeter
  ElectronFilter
  TrackPileUpSubtractor
  NeutralTowerMerger
  EFlowMergerAllTracks
  EFlowMerger
  EFlowFilter

  NeutrinoFilter
  GenJetFinder
  GenMissingET
```

```
    Rho
    FastJetFinder
    JetPileUpSubtractor

    JetEnergyScale

    PhotonEfficiency
    PhotonIsolation

    ElectronEfficiency
    ElectronIsolation

    MuonEfficiency
    MuonIsolation

    JetFlavorAssociation

    BTagging
    TauTagging

    UniqueObjectFinder

    MissingET

    ScalarHT

    TreeWriter
}

############
# Missing ET merger
############
# Several InputArray added to Missing ET Merger

module Merger MissingET {
    # add InputArray InputArray
    # add InputArray EFlowMergerAllTracks/eflow
    # added:
    add InputArray UniqueObjectFinder/jets
    add InputArray UniqueObjectFinder/electrons
    add InputArray UniqueObjectFinder/photons
    add InputArray UniqueObjectFinder/muons
    set MomentumOutputArray momentum
}
```

```
############
# MC truth jet finder
############
# Values changed for ParameterR and JetPTMin

module FastJetFinder GenJetFinder {
    set InputArray NeutrinoFilter/filteredParticles

    set OutputArray jets

    # algorithm: 1 CDFJetClu, 2 MidPoint, 3 SIScone, 4 kt, 5 Cambridge/Aachen, 6 antikt
    set JetAlgorithm 6

    set ParameterR 0.4

    set JetPTMin 30.0
}

#######
# Jet finder
#######
# Values changed for ParameterR and JetPTMin

module FastJetFinder FastJetFinder {
    set InputArray Calorimeter/towers

    set OutputArray jets

    # area algorithm: 0 Do not compute area, 1 Active area explicit ghosts, 2 One ghost passive
area, 3 Passive area, 4 Voronoi, 5 Active area
    set AreaAlgorithm 5

    # jet algorithm: 1 CDFJetClu, 2 MidPoint, 3 SIScone, 4 kt, 5 Cambridge/Aachen, 6 antikt
    set JetAlgorithm 6

    set ParameterR 0.4

    set JetPTMin 30.0
}

##############
# Jet Pile-Up Subtraction
##############
# Values changed for JetPTMin

module JetPileUpSubtractor JetPileUpSubtractor {
    set JetInputArray FastJetFinder/jets
    set RhoInputArray Rho/rho
```

```
    set OutputArray jets

    set JetPTMin 30.0
}

#################
# Electron tracking efficiency
#################
# Altered to include different efficiency to account for calorimeter crack from abs(eta) = 1.2 to 1.5

module Efficiency ElectronTrackingEfficiency {
    set InputArray ParticlePropagator/electrons
    set OutputArray electrons

    # set EfficiencyFormula {efficiency formula as a function of eta and pt}

    # tracking efficiency formula for electrons
     set EfficiencyFormula        { (pt <= 0.1) * (0.00) +
       (abs(eta) <= 0.1) * (0.90) +
       (abs(eta) > 0.1 && abs(eta) <= 1.2) * (pt > 0.1 && pt <= 1.0) * (0.73) +
       (abs(eta) > 0.1 && abs(eta) <= 1.2) * (pt > 1.0 && pt <= 1.0e2) * (0.95) +
       (abs(eta) > 0.1 && abs(eta) <= 1.2) * (pt > 1.0e2) * (0.99) +
       (abs(eta) > 1.2 && abs(eta) <= 1.5) * (pt > 0.1 && pt <= 1.0) * (0.73) +
       (abs(eta) > 1.2 && abs(eta) <= 1.5) * (pt > 1.0 && pt <= 1.0e2) * (0.95) +
       (abs(eta) > 1.2 && abs(eta) <= 1.5) * (pt > 1.0e2) * (0.99) +
       (abs(eta) > 1.5 && abs(eta) <= 2.5) * (pt > 0.1 && pt <= 1.0) * (0.50) +
       (abs(eta) > 1.5 && abs(eta) <= 2.5) * (pt > 1.0 && pt <= 1.0e2) * (0.83) +
       (abs(eta) > 1.5 && abs(eta) <= 2.5) * (pt > 1.0e2) * (0.99) +
       (abs(eta) > 2.5) * (0.00)}
}
```

Appendix B

On the relative difference between two independent histograms

Consider a histogram h_1 with bin content a_j and error σ_{aj}, and another histogram h_2 with content b_j and error σ_{bj} for bin j. Assuming that $\mathrm{cov}(a_j, b_j) = 0$, the relative difference between h_1 and h_2 for a given bin is [46]

$$\epsilon = \frac{d}{s} \tag{B.1}$$

where $d = b - a$, and

$$s = \frac{\frac{a}{\sigma_a^2} + \frac{b}{\sigma_b^2}}{\frac{1}{\sigma_a^2} + \frac{1}{\sigma_b^2}} \tag{B.2}$$

is the maximum likelihood estimate of the bin content, assuming they are both from a common true histogram. Then

$$\frac{1}{\sigma_s^2} = \frac{1}{\sigma_a^2} + \frac{1}{\sigma_b^2}. \tag{B.3}$$

Assuming a and b fluctuate with fixed variances σ_a^2 and σ_b^2, then

$$\begin{aligned} \mathrm{cov}(d, s) &= \langle ds \rangle - \langle d \rangle \langle s \rangle \\ &= \left\langle (b-a) \left(\frac{a}{\sigma_a^2} + \frac{b}{\sigma_b^2} \right) \sigma_s^2 \right\rangle - \langle b - a \rangle \left\langle \left(\frac{a}{\sigma_a^2} + \frac{b}{\sigma_b^2} \right) \sigma_s^2 \right\rangle \\ &= \left(\langle b^2 \rangle - \langle b \rangle^2 \right) \frac{\sigma_s^2}{\sigma_b^2} - \left(\langle a^2 \rangle - \langle a \rangle^2 \right) \frac{\sigma_s^2}{\sigma_a^2} + \left(\langle ab \rangle - \langle a \rangle \langle b \rangle \right) \left(\frac{\sigma_s^2}{\sigma_a^2} - \frac{\sigma_s^2}{\sigma_b^2} \right) \end{aligned} \tag{B.4}$$

but, $\mathrm{cov}(a,b) = \langle ab \rangle - \langle a \rangle \langle b \rangle = 0$. So,

$$\mathrm{cov}(d,s) = \sigma_b^2 \left(\frac{\sigma_s^2}{\sigma_b^2} \right) - \sigma_a^2 \left(\frac{\sigma_s^2}{\sigma_a^2} \right) = 0 \tag{B.5}$$

meaning that s and d are uncorrelated. Therefore, for one bin, using error propagation,

$$\begin{aligned} \left(\frac{\sigma_\epsilon}{\epsilon} \right)^2 &= \left(\frac{\sigma_d}{d} \right)^2 + \left(\frac{\sigma_s}{s} \right)^2 \\ &= \frac{\sigma_a^2 + \sigma_b^2}{(b-a)^2} + \frac{\sigma_s^2}{s^2}. \end{aligned} \tag{B.6}$$

Now, using Equation B.2,

$$s = \frac{\frac{a}{\sigma_a^2} + \frac{b}{\sigma_b^2}}{\frac{1}{\sigma_a^2} + \frac{1}{\sigma_b^2}} = \frac{a\sigma_b^2 + b\sigma_a^2}{\sigma_a^2 + \sigma_b^2}, \text{ and} \tag{B.7}$$

$$\sigma_s^2 = \frac{1}{\frac{1}{\sigma_a^2} + \frac{1}{\sigma_b^2}} = \frac{\sigma_a^2 \sigma_b^2}{\sigma_a^2 + \sigma_b^2}. \tag{B.8}$$

So, from Equation B.6,

$$\begin{aligned} \left(\frac{\sigma_\epsilon}{\epsilon} \right)^2 &= \frac{\sigma_a^2 + \sigma_b^2}{(b-a)^2} + \frac{\sigma_a^2 \sigma_b^2 (\sigma_a^2 + \sigma_b^2)}{(a\sigma_b^2 + b\sigma_a^2)^2} \\ &= \frac{a^2\sigma_b^2 + b^2\sigma_a^2}{(b-a)^2 s^2}. \end{aligned} \tag{B.9}$$

So,

$$\sigma_\epsilon = \frac{\sqrt{a^2\sigma_b^2 + b^2\sigma_a^2}}{s^2}. \tag{B.10}$$

Now, for bin j,

$$\epsilon_j = \frac{d_j}{s_j} = \frac{b_j - a_j}{s_j} \tag{B.11}$$

where

$$s_j = \frac{\frac{a_j}{\sigma_{aj}^2} + \frac{b_j}{\sigma_{bj}^2}}{\frac{1}{\sigma_{aj}^2} + \frac{1}{\sigma_{bj}^2}}. \tag{B.12}$$

Then

$$\sigma_{\epsilon j}^2 = \frac{a_j^2 \sigma_{bj}^2 + b_j^2 \sigma_{aj}^2}{s_j^4}. \tag{B.13}$$

Then the average relative difference is given by

$$\langle \epsilon \rangle = \frac{\sum_j \frac{\epsilon_j}{\sigma_{\epsilon j}^2}}{\sum_j \frac{1}{\sigma_{\epsilon j}^2}}, \tag{B.14}$$

the absolute of the average relative difference is

$$\langle |\epsilon| \rangle = \frac{\sum_j \left| \frac{\epsilon_j}{\sigma_{\epsilon j}^2} \right|}{\sum_j \frac{1}{\sigma_{\epsilon j}^2}}, \tag{B.15}$$

and the root mean square relative difference is expressed as

$$\delta_\epsilon = \sqrt{\langle \epsilon^2 \rangle} = \sqrt{\frac{\sum_j \frac{\epsilon_j^2}{\sigma_{\epsilon j}^2}}{\sum_j \frac{1}{\sigma_{\epsilon j}^2}}}. \tag{B.16}$$

Appendix C

Extra kinematic distributions

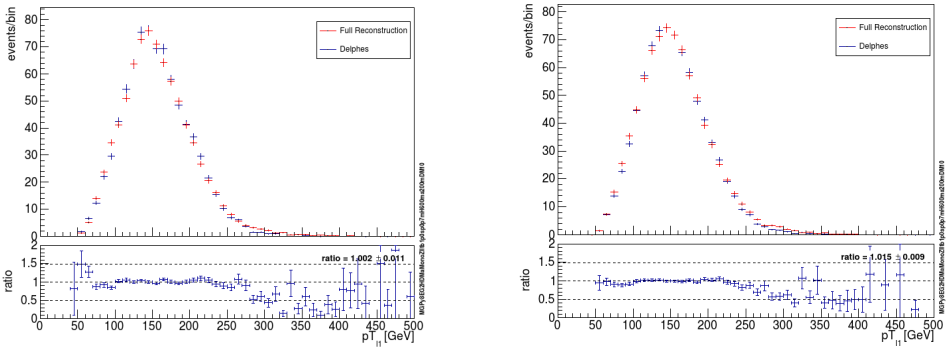

(a) ee channel. (b) $\mu\mu$ channel.

Figure C.1: p_T of leading lepton for ee and $\mu\mu$ channels, for $\sin\theta = 0.7$.

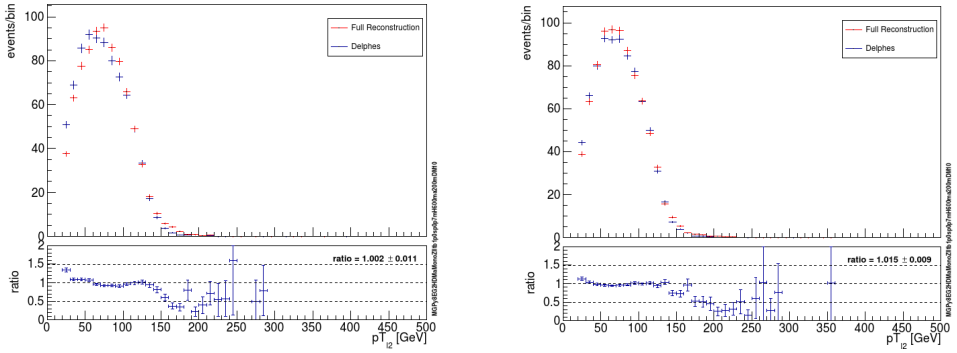

(a) ee channel. (b) $\mu\mu$ channel.

Figure C.2: p_T of subleading lepton for ee and $\mu\mu$ channels, for $\sin\theta = 0.7$.

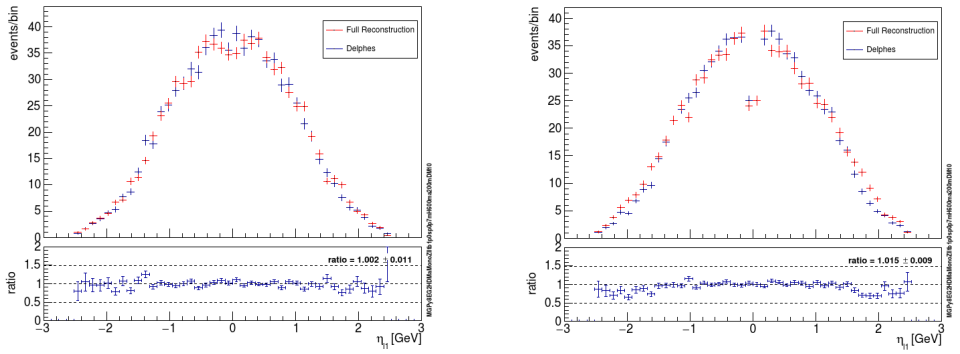

(a) ee channel. (b) $\mu\mu$ channel.

Figure C.3: η of leading lepton for ee and $\mu\mu$ channels, for $\sin\theta = 0.7$.

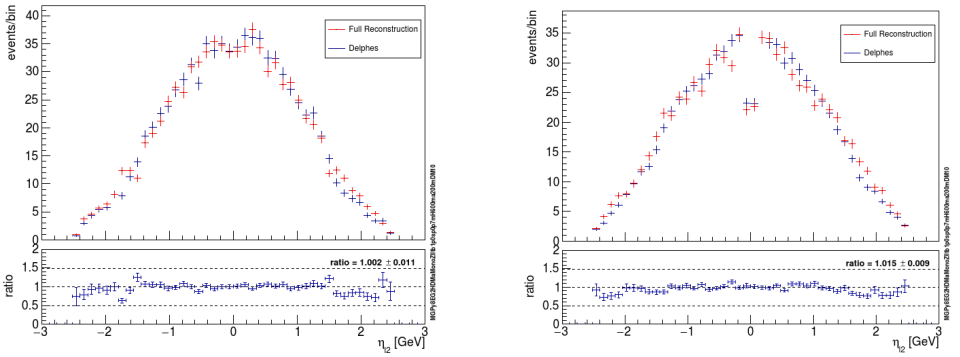

(a) ee channel. (b) $\mu\mu$ channel.

Figure C.4: η of subleading lepton for ee and $\mu\mu$ channels, for $\sin\theta = 0.7$.

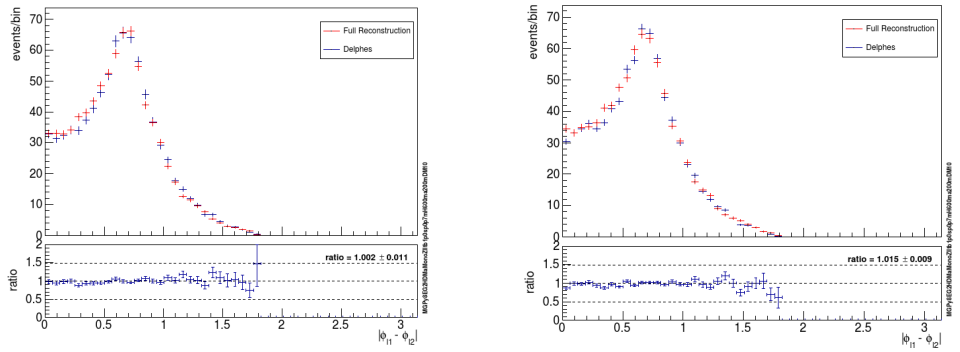

(a) ee channel. (b) $\mu\mu$ channel.

Figure C.5: Azimuthal separation between leptons for ee and $\mu\mu$ channels, for $\sin\theta = 0.7$.

Appendix D

m_{TZZ} distributions for systematics case 2

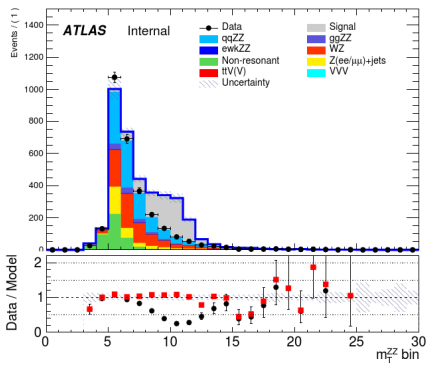

(a) Pre-fit m_{TZZ} distribution.

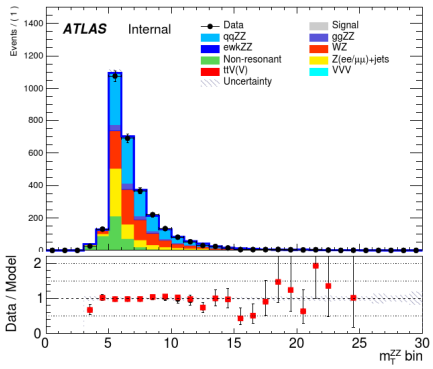

(b) Post-fit m_{TZZ} distribution.

Figure D.1: Pre- and post-fit m_{TZZ} distributions for ee channel for $\sin\theta = 0.7$.

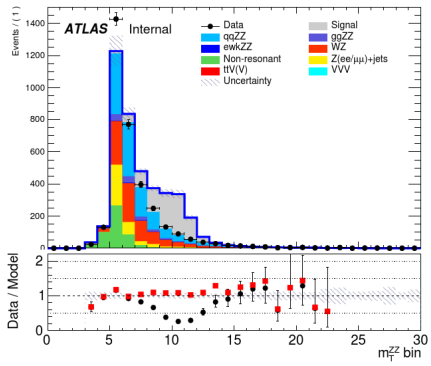

(a) Pre-fit m_{TZZ} distribution.

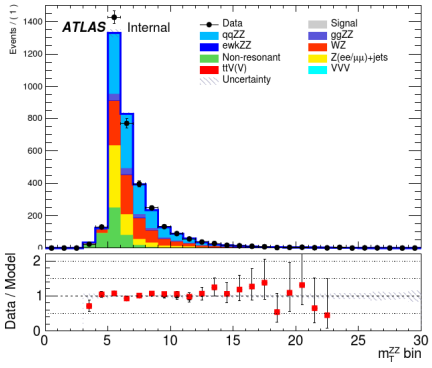

(b) Post-fit m_{TZZ} distribution.

Figure D.2: Pre- and post-fit m_{TZZ} distributions for $\mu\mu$ channel for $\sin\theta = 0.7$.

Bibliography

[1] Particle Data Group collaboration, P. Zyla et al., *Review of Particle Physics*, *PTEP* **2020** (2020) 083C01.

[2] ATLAS collaboration, G. Aad, T. Abajyan, B. Abbott, J. Abdallah, S. Abdel Khalek, A. Abdelalim et al., *Observation of a New Particle in the Search for the Standard Model Higgs Boson with the ATLAS Detector at the LHC*, *Physics Letters B* **716** (Sep, 2012) 1–29, [1207.7214].

[3] CMS collaboration, S. Chatrchyan, V. Khachatryan, A. Sirunyan, A. Tumasyan, W. Adam, E. Aguilo et al., *Observation of a new boson at a mass of 125 GeV with the CMS experiment at the LHC*, *Physics Letters B* **716** (Sep, 2012) 30–61, [1207.7235].

[4] C. Grojean, *Higgs Physics*, *CERN Yellow Report* (Aug, 2017) 143–158, [1708.00794].

[5] ATLAS collaboration, M. Aaboud, G. Aad, B. Abbott, J. Abdallah, O. Abdinov, B. Abeloos et al., *Measurement of the ZZ production cross section in proton-proton collisions at $\sqrt{s} = 8$ TeV using the $ZZ \to \ell^-\ell^+\ell'^-\ell'^+$ + and $ZZ \to \ell^-\ell^+\nu\overline{\nu}$ decay channels with the ATLAS detector*, *Journal of High Energy Physics* **2017** (Jan, 2017) .

[6] J. P. Ellis, *TikZ-Feynman: Feynman diagrams with TikZ*, Jan, 2017. 10.1016/j.cpc.2016.08.019.

[7] K. Kumerički, *Feynman Diagrams for Beginners*, 1602.04182.

[8] D. J. Griffiths, *Introduction to elementary particles; 2nd rev. version*. Physics textbook. Wiley, New York, NY, 2008.

[9] A. V. Zasov, A. S. Saburova, A. V. Khoperskov and S. A. Khoperskov, *Dark matter in galaxies*, *Physics-Uspekhi* **60** (Jan, 2017) 3, [1710.10630].

[10] V. Belokurov, N. W. Evans, A. Moiseev, L. J. King, P. C. Hewett, M. Pettini et al., *The Cosmic Horseshoe: discovery of an Einstein ring around a giant luminous red galaxy*, *The Astrophysical Journal* **671** (Nov, 2007) , [0706.2326].

[11] M. Markevitch, A. H. Gonzalez, D. Clowe, A. Vikhlinin, W. Forman, C. Jones et al., *Direct Constraints on the Dark Matter Self Interaction Cross Section from the Merging Galaxy Cluster 1E 0657 56*, *The Astrophysical Journal* **606** (May, 2004) 819824.

[12] R. Thompson, R. Davé and K. Nagamine, *The rise and fall of a challenger: the Bullet Cluster in Λ cold dark matter simulations*, *Monthly Notices of the Royal Astronomical Society* **452** (Jul, 2015) 3030–3037, [1410.7438].

[13] J. R. Brownstein and J. W. Moffat, *The Bullet Cluster 1E0657-558 evidence shows modified gravity in the absence of dark matter*, *Monthly Notices of the Royal Astronomical Society* **382** (Nov, 2007) 29–47.

[14] P. F. Michelson, W. B. Atwood and S. Ritz, *Fermi Gamma-ray Space Telescope: high-energy results from the first year*, *Reports on Progress in Physics* **73** (Jun, 2010) 074901, [1011.0213].

[15] E. Aprile, J. Aalbers, F. Agostini, M. Alfonsi, L. Althueser, F. Amaro et al., *Search for inelastic scattering of WIMP dark matter in XENON1T*, *Physical Review D* **103** (Mar, 2021) 063028, [2011.10431].

[16] M. Felcini, *Searches for Dark Matter Particles at the LHC*, 1809.06341.

[17] J. Haffner, *The CERN accelerator complex. Complexe des accélérateurs du CERN*, Oct, 2013.

[18] ATLAS collaboration, M. E. Pozo Astigarraga, *The ATLAS Data Acquisition System in LHC Run 2*, tech. rep., CERN, Geneva, Nov, 2017.

[19] E. Stanecka, *The ATLAS Inner Detector operation, data quality and tracking performance*, 1303.3630.

[20] ATLAS collaboration, M. Aaboud, G. Aad, B. Abbott, O. Abdinov, B. Abeloos, S. Abidi et al., *Search for an invisibly decaying Higgs boson or dark matter candidates produced in association with a Z boson in pp collisions at* $\sqrt{s}$

= *13 TeV with the ATLAS detector*, *Phyics Letters B* **318** (Jan, 2017) 318–337, [1708.09624].

[21] ATLAS collaboration, G. Aad, E. Abat, B. Abbott, J. Abdallah, A. A. Abdelalim, A. Abdesselam et al., *Performance of the ATLAS detector using first collision data*, *Journal of High Energy Physics* **2010** (Sep, 2010) , [1005.5254].

[22] ATLAS collaboration, G. Aad, B. Abbott, J. Abdallah, A. A. Abdelalim, A. Abdesselam, O. Abdinov et al., *The ATLAS Inner Detector commissioning and calibration*, *The European Physical Journal C* **70** (Aug, 2010) 787–821, [1004.5293].

[23] ATLAS collaboration, G. Aad et al., *The ATLAS Experiment at the CERN Large Hadron Collider*, *Journal of Instrumentation* **3** (2008) S08003.

[24] J. Abdallah, *Upgraded electronics of the ATLAS hadronic Tile Calorimeter for the High Luminosity LHC*, *Journal of Instrumentation* **15** (Jun, 2020) C06048, [2002.06427].

[25] ATLAS Liquid Argon Calorimeter collaboration, H.-Q. Zhang, *The ATLAS Liquid Argon calorimeter: Overview and performance*, *J. Phys. Conf. Ser.* **293** (2011) 012044.

[26] ATLAS collaboration, G. Aad, B. Abbott, J. Abdallah, A. A. Abdelalim, A. Abdesselam, O. Abdinov et al., *Commissioning of the ATLAS Muon Spectrometer with cosmic rays*, *The European Physical Journal C* **70** (Oct, 2010) 875–916, [1006.4384].

[27] E. Diehl, *Calibration and Performance of the ATLAS Muon Spectrometer*, 1109.6933.

[28] ATLAS collaboration, *Operation of the ATLAS trigger system in Run 2*, *Journal of Instrumentation* **15** (Oct, 2020) P10004, [12007.12539].

[29] R. Reed, *The Upgrade of the ATLAS Tile Calorimeter Readout Electronics for Phase II*, *Journal of Physics Conference Series 1742-6588* **623** (Dec, 2014) 012024.

[30] CMS collaboration, S. Chatrchyan, V. Khachatryan, A. M. Sirunyan, A. Tumasyan, W. Adam, T. Bergauer et al., *Search for New Physics with a Mono-Jet and Missing Transverse Energy in pp Collisions at $\sqrt{s} = 7$ TeV*, *Physical Review Letters* **107** (Nov, 2011) 201804, [1106.4775].

[31] A. Berlin, T. Lin and L.-T. Wang, *Mono-Higgs Detection of Dark Matter at the LHC*, *Journal of High Energy Physics* **2014** (Jun, 2014) , [1402.7074].

[32] J. Abdallah, H. Araujo, A. Arbey, A. Ashkenazi, A. Belyaev, J. Berger et al., *Simplified models for dark matter searches at the LHC*, *Physics of the Dark Universe* **9-10** (Sep, 2015) 8–23, [1506.03116].

[33] A. Elliot, *Search for dark matter produced in association with a leptonically decaying Z boson in the ATLAS detector at the Large Hadron Collider*. PhD thesis, University of Victoria, Aug, 2017.

[34] M. Bauer, U. Haisch and F. Kahlhoefer, *Simplified dark matter models with two Higgs doublets: I. Pseudoscalar mediators*, *Journal of High Energy Physics* **2017** (May, 2017) , [1701.07427].

[35] S. Ipek, D. McKeen and A. E. Nelson, *A Renormalizable Model for the Galactic Center Gamma Ray Excess from Dark Matter Annihilation*, *Physical Review D* **90** (Sep, 2014) 055021, [1404.3716].

[36] A. Biswas and A. Lahiri, *Masses of physical scalars in two Higgs doublet models*, *Physical Review D* **91** (Jun, 2015) 115012, [1412.6187].

[37] B. Penning, *The Pursuit of Dark Matter at Colliders - An Overview*, *Journal of Physics G: Nuclear and Particle Physics* **45** (May, 2018) 063001, [1712.01391].

[38] A. Sirunyan, A. Tumasyan, W. Adam, F. Ambrogi, E. Asilar, T. Bergauer et al., *Performance of missing transverse momentum reconstruction in proton-proton collisions at $\sqrt{s} = 13$ TeV using the CMS detector*, *Journal of Instrumentation* **14** (Jul, 2019) P07004, [1903.06078].

[39] ATLAS collaboration, *Object-based missing transverse momentum significance in the ATLAS detector*, tech. rep., CERN, Geneva, Jul, 2018.

[40] CMS collaboration, S. C. et al., *The CMS experiment at the CERN LHC*, *Journal of Instrumentation* **3** (2008) S08004.

[41] K. McLean, *Search for dark matter produced in association with a Z boson in the ATLAS detector at the Large Hadron Collider*. PhD thesis, University of Victoria, 2021.

[42] J. Alwall, M. Herquet, F. Maltoni, O. Mattelaer and T. Stelzer, *MadGraph5: Going Beyond*, *Journal of High Energy Physics* **06** (Jun, 2011) , [1106.0522].

[43] C. Bierlich, N. Desai, L. Gellersen, I. Helenius, P. Ilten, L. Lönnblad et al., *PYTHIA (version 8.303)*, 2020.

[44] C. Delaere, M. Selvaggi, P. Demin, P. Lemaître, J. de Favereau, A. Giammanco et al., *DELPHES: fast simulation (version 3.4.2)*, 2019.

[45] J. de Favereau, C. Delaere, P. Demin, A. Giammanco, V. Lemaitre, A. Mertens et al., *DELPHES 3: A modular framework for fast simulation of a generic collider experiment*, *Journal of High Energy Physics* **2014** (Feb, 2014) , [1307.6346].

[46] M. Lefebvre, *private communication*, 2021.

[47] N. Gagunashvili, *Pearson's Test Modifications for Comparison of Unweighted and Weighted Histograms and Two Weighted Histograms*, *PoS* **ACAT** (2009) 060.

[48] K. Cranmer, *Practical Statistics for the LHC*, 1503.07622.

[49] G. Cowan, K. Cranmer, E. Gross and O. Vitells, *Asymptotic formulae for likelihood-based tests of new physics*, *The European Physical Journal C* **71** (Feb, 2013) , [1007.1727].

[50] A. Wald, *Tests of Statistical Hypotheses Concerning Several Parameters When the Number of Observations is Large*, *Transactions of the American Mathematical Society* **54** (1943) 426–482.

[51] M. Baak, G. J. Besjes, D. Côté, A. Koutsman, J. Lorenz and D. Short, *HistFitter software framework for statistical data analysis*, *The European Physical Journal C* **75** (Apr, 2014) , [1410.1280].